





Optimizing post-Newtonian parameters and fixing the BMS frame for numerical-relativity waveform hybridizations

Dongze Sun ^{1,*} Michael Boyle ² Keefe Mitman ¹

Mark A. Scheel ¹ Leo C. Stein ³ Saul A. Teukolsky ^{1,2} and Vijay Varma ^{4,5}

¹*Theoretical Astrophysics 350-17, California Institute of Technology, 1200 E California Boulevard, Pasadena, CA 91125, USA*

²*Cornell Center for Astrophysics and Planetary Science, Cornell University, Ithaca, New York 14853, USA*

³*Department of Physics and Astronomy, University of Mississippi, University, MS 38677, USA*

⁴*Department of Mathematics, Center for Scientific Computing and Visualization*

Research, University of Massachusetts, Dartmouth, MA 02747, USA

⁵*Max Planck Institute for Gravitational Physics (Albert Einstein Institute), D-14476 Potsdam, Germany*

(Dated: March 18, 2024)

Numerical relativity (NR) simulations of binary black holes provide precise waveforms, but are typically too computationally expensive to produce waveforms with enough orbits to cover the whole frequency band of gravitational-wave observatories. Accordingly, it is important to be able to hybridize NR waveforms with analytic, post-Newtonian (PN) waveforms, which are accurate during the early inspiral phase. We show that to build such hybrids, it is crucial to both fix the Bondi-Metzner-Sachs (BMS) frame of the NR waveforms to match that of PN theory, and optimize over the PN parameters. We test such a hybridization procedure including all spin-weighted spherical harmonic modes with $|m| \leq \ell$ for $\ell \leq 8$, using 29 NR waveforms with mass ratios $q \leq 10$ and spin magnitudes $|\chi_1|, |\chi_2| \leq 0.8$. We find that for spin-aligned systems, the PN and NR waveforms agree very well. The difference is limited by the small nonzero orbital eccentricity of the NR waveforms, or equivalently by the lack of eccentric terms in the PN waveforms. To maintain full accuracy of the simulations, the matching window for spin-aligned systems should be at least 5 orbits long and end at least 15 orbits before merger. For precessing systems, the errors are larger than for spin-aligned cases. The errors are likely limited by the absence of precession-related spin-spin PN terms. Using $10^5 M$ long NR waveforms, we find that there is no optimal choice of the matching window within this time span, because the hybridization result for precessing cases is always better if using earlier or longer matching windows. We provide the mean orbital frequency of the smallest acceptable matching window as a function of the target error between the PN and NR waveforms and the black hole spins.

I. INTRODUCTION

Gravitational-wave (GW) astronomy has revealed previously unattainable details about the astrophysics of compact objects [1–9] and the behavior of gravity in extreme regimes [10–12], thanks to the collaboration of LIGO, Virgo, and KAGRA [13–16]. To further advance the field, the next generation of ground-based detectors, such as the Einstein Telescope (ET) [17] and Cosmic Explorer (CE) [18], as well as the first-generation of space-based detectors, including LISA [19], TianQin [20], and Taiji [21], are currently under development. These detectors are expected to provide a significant increase in sensitivity and bandwidth, enabling the detection of GW signals at frequencies as low as 0.1 mHz [22–24].

To fully exploit the scientific potential of these gravitational-wave observations, it is essential to construct precise theoretical waveform templates. The most accurate waveform templates are obtained through numerical simulations of the full set of Einstein’s equations of general relativity, which is known as numerical relativity (NR). However, NR simulations are typically too computationally expensive to produce waveforms with

enough orbits to cover the whole frequency band that is detectable by gravitational-wave observatories. Alternatively, analytic models based on the post-Newtonian (PN) approximation are efficient at providing waveforms that cover the low-frequency band during the early inspiral phase of binary black hole (BBH) systems. However, PN waveforms are not accurate for the late inspiral and merger phases of BBH systems. Consequently, it is important to be able to attach a PN waveform to the beginning of an NR waveform, thus producing a *hybrid* waveform that is accurate for the entire frequency band of GW detectors.

Such hybrid models were developed for example, in Refs. [25–30]. These models attained mismatches of 10^{-4} between the hybrid and NR waveforms in the matching window (for $m \neq 0$ modes) for non-precessing systems [29], and between 10^{-2} and 10^{-1} (for $m \neq 0$ modes) for precessing systems [30]. However, these models have four major limitations: (1) They did not account for the $m = 0$ modes since their NR waveforms did not include the correct gravitational-wave memory contribution. (2) The NR waveforms used in these models were not in the same frame as the PN waveforms. Reference [31] showed that comparing CCE waveforms without fixing the gauge freedom can result in relative errors three orders of magnitude larger than if one first fixes such freedoms. And they also showed that comparing CCE waveforms after mapping

* dzsun@caltech.edu

them to the same BMS frame can achieve smaller errors than comparing the extrapolated waveforms. Furthermore, Ref. [31] successfully developed a hybrid model that incorporates memory-containing waveforms. (3) These models used NR values of masses and spins to compute the corresponding PN waveform. As we will demonstrate in this paper, the NR values of these parameters differ from the PN values that minimize mismatch. (4) Existing models are primarily applicable to spin-aligned or anti-aligned systems, such as binaries born from isolated stellar evolution [32–34]. The accuracy of hybridization for precessing systems is severely limited by the inaccurate methodology previously mentioned: the mismatch is on the order of 10^{-2} or higher [30]. Theoretical considerations [32, 34] and observational evidence [9, 35, 36] indicate that spins can be randomly oriented for binaries that form dynamically in dense environments, and even binaries formed in isolation can exhibit distinctive precessional dynamics. Therefore, it is crucial to develop accurate hybrid models that are valid for precessing systems.

One technique that enables the extraction of waveforms at null infinity is Cauchy-characteristic evolution (CCE) [37–41]. It uses a worldtube from the Cauchy evolution of the Einstein field equations as the inner boundary to a characteristic evolution along null rays. The gravitational information is propagated and evolved to future null infinity, so one can obtain waveforms in any desired gauge. Reference [31] has shown that by mapping the CCE waveform to the correct Bondi-Metzner-Sachs (BMS) frame, the NR waveform agrees much better with that of PN. A key advantage of the hybrid waveforms presented here is that we use CCE NR waveforms. By contrast, previous hybrid waveform models [25–30] used NR waveforms that were computed at null infinity using an extrapolation technique [42] that does not have a well-defined BMS frame and does not yield the correct memory contribution.

In this work, we simultaneously optimize over the PN parameters and fix the BMS frame of NR waveforms to build hybrid waveforms. The optimization and the fixing of the BMS frame, which includes the alignment of the rotation and time shift, are performed inside a time interval called a *matching window*. Because we use CCE and thus obtain the correct gravitational-wave memory, we are able to include all $-\ell \leq m \leq \ell$ for $\ell \leq 8$ spin-weighted spherical harmonic modes in the hybrid waveforms. We test the hybridization procedure using 29 NR waveforms from the SXS catalog [43] with mass ratios $q \leq 10$ and $|\chi_1|, |\chi_2| \leq 0.8$. The length of these waveforms ranges from 60 to over 100 orbits, making it possible to test the hybrid waveforms by comparing them to long NR waveforms at a very early stage. We find that for spin-aligned systems, we can reduce the PN–NR mismatches to the error caused by small non-zero eccentricities of the NR systems. We achieve a mismatch (in a 10-orbit long matching window ending $8000 M$ before merger) around two to three orders of magnitude smaller than previous models [25–29]. For precessing systems, we

find that hybridization is likely limited by the absence of precession-related spin-spin PN terms, yielding mismatches one to two orders of magnitude smaller than previous models [44].

This paper is organized as follows. In Sec. II, we introduce the PN and NR waveforms that we use to build the hybrid waveforms, and we discuss the freedoms in the physical parameters, 3D rotations and time shift, and further BMS frame parameters not previously considered. In Sec. III, we explain how we match the physical parameters and inertial frames between NR and PN waveforms. Following this, we present the complete procedure to build the hybrid waveforms in Sec. IV. In Sec. V, we show the hybridization results as well as the improvement from PN parameters and BMS frame fixing compared with previous models, and we use the findings to more precisely compare the PN and NR waveforms. Sec. VI analyzes the sources of error for spin-aligned and precessing systems. Additionally, based on our error analysis, we make recommendations for future surrogate models’ matching window selection in Sec. VII. In Sec. VIII, we provide a few closing remarks. We make the code used for this hybridization procedure publicly available in Ref. [45].

II. WAVEFORMS

The complex strain $h = h_+ - ih_\times$ is decomposed into modes according to

$$h(u, \theta, \phi) = \sum_{\ell=2}^{\infty} \sum_{m=-\ell}^{\ell} h_{\ell m}(u) {}_{-2}Y_{\ell m}(\theta, \phi), \quad (1)$$

where $u \equiv t - r$ is the retarded time and ${}_{-2}Y_{\ell m}$ are the spin-weight -2 spherical harmonics. We model all the $-\ell \leq m \leq \ell$ modes for $\ell \leq 8$.

A. Post-Newtonian waveforms

In this study, we use PN theory to describe the GW waveforms of BBHs in quasi-circular orbits during the early inspiral stage, and include GW memory contributions. Memory effects should be inherent in any correct PN formulation, but their importance can often be overlooked. In our case, we find that accounting for memory is crucial when comparing to NR waveforms that have memory, and thus crucial for accurate hybridization.

For binding energy and flux, we include nonspinning terms that are complete to 3.5 PN order from [46], and also the 4 PN terms from [47]. We also include higher-order terms up to 6 PN from [48], but these terms are obtained in the EMRI limit. We include the spin-orbit terms up to 4 PN order from [49], spin-spin terms up to 3 PN order from [50], and 3.5 PN spin-cubed terms from [51] for the orbital phase.

For the precession of spins and the orbital angular momentum, we include spin-orbit terms up to 3.5 PN from [52], and spin-spin terms up to 4 PN from [50].

For mode amplitudes, we include terms up to 4 PN. The terms up to 3 PN are taken from [53], the 3.5 PN terms in the (2, 2) mode and $\ell = 3$ modes are taken from [54] and [55], respectively, and the 4 PN terms in (2, 2) mode are taken from [47]. We also include memory terms up to 3 PN [31] for mode amplitudes.

We also generate the PN Moreschi supermomentum [56], which we will later use to fix the BMS frame of NR systems, as we will detail in Sec. II B. The Moreschi supermomentum modes are taken from [31]. We leave the effects of eccentric orbits for discussion in Sec. VI.

To produce the PN phase as a function of time, we use the TaylorT1 approximant. The PN generation is implemented in the Python package `NRPNHybridization` [45].

There are 8 independent physical parameters in quasi-circular PN theory: mass ratio q , total mass M , and two three-dimensional spin vectors χ_1 and χ_2 . The remaining parameters are all gauge. There are 4 parameters for a time shift and SO(3) rotation, which were considered in previous hybridization work. The rest of the BMS group includes a Lorentz boost (3 parameters), and a supertranslation (described below), which is given by a smooth real-valued function $\alpha(\theta, \phi)$ on the sphere. We band-limit α to $\ell \leq 8$ modes, and its (0,0) mode is already accounted for in the time shift above, so α contributes an additional $(\ell + 1)^2 - 1 = 80$ real parameters.

B. Numerical-relativity waveforms and BMS frames

It is worth noting that models of gravitational-wave emission are usually constructed in asymptotically flat spacetimes. Bondi, van der Burg, Metzner, and Sachs [57–59] demonstrated that the spacetime symmetry at the asymptotic boundary is the BMS group. This is comprised of the usual Lorentz transformations, as well as a set of generalized time and space translations referred to as “supertranslations,” which can be interpreted as direction-dependent translations on the asymptotic boundary. Specifically, under a supertranslation $\alpha(\theta, \phi)$, the retarded-time coordinate $u \equiv t - r$ transforms as

$$u' = u - \alpha(\theta, \phi). \quad (2)$$

These transformations are implemented in the `scri` python package [60], using the method described in Ref. [61].

Reference [62] emphasized the importance of having both PN and NR waveforms in the same BMS frame. We follow their procedure to map NR waveforms to the corresponding PN BMS frame. First, we determine the space translation and boost by minimizing the center-of-mass charge. We then calculate the supertranslations that map the $\ell \leq 2$ modes of the NR Moreschi supermomentum Ψ_M^{NR} to the corresponding PN Moreschi supermomentum

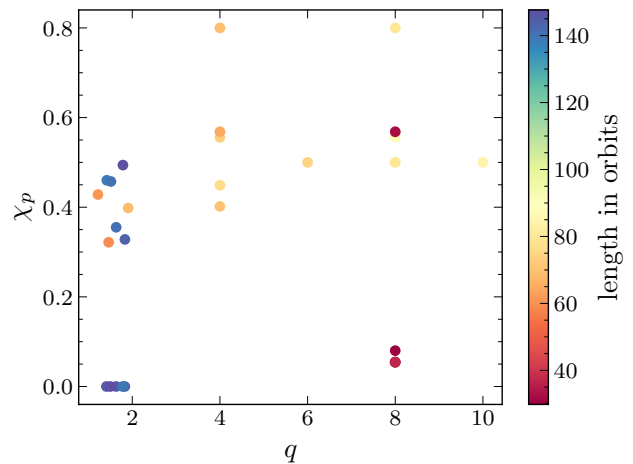


FIG. 1. The parameter space of the NR simulations that we use. The color shows the length of the waveform in terms of orbits.

Ψ_M^{PN} , where Ψ_M is

$$\Psi_M \equiv \Psi_2 + \sigma \bar{\sigma} + \bar{\delta}^2 \bar{\sigma}, \quad (3)$$

with Ψ_2 being the Weyl scalar with spin-weight 0, σ the Newman-Penrose shear, and an overbar representing complex conjugation. For a quantity η of spin weight s , the spin-weight raising operator $\bar{\delta}$ is defined as [63, 64]

$$\bar{\delta}\eta = -\frac{1}{\sqrt{2}}(\sin\theta)^s \left(\frac{\partial}{\partial\theta} + \frac{i}{\sin\theta} \frac{\partial}{\partial\phi} \right) ((\sin\theta)^{-s}\eta). \quad (4)$$

The mapping to the BMS frame is done using an iterative procedure [31, 62], as we explain in more detail below in Sec. IV.

We use NR waveforms that are computed using a Cauchy-characteristic evolution (CCE) [40, 41], for which the Cauchy evolution parts are performed using the Spectral Einstein Code (SpEC) [65], and the CCE computation is performed using the SpECTRE code [66]. CCE uses a worldtube from the Cauchy evolution of the Einstein field equations as the inner boundary of a characteristic evolution on a null foliation. The gravitational information is propagated and evolved to future null infinity. Note that Ψ_2 and σ required in Eq. (3) are calculated by the SpECTRE CCE code.

The NR waveforms that we use are from simulations in the SXS catalog [43]. We plot the parameter space χ_p versus q in Fig. 1, where $\chi_p = \max\{\chi_{1\perp}, \frac{4+3q}{q(4q+3)}\chi_{2\perp}\}$ [67] and $\chi_{1,2\perp}$ is the magnitude of the projection in the orbital plane. They are systems SXS:BBH:1412–1416 and 2617–2640. Of these, SXS:BBH:1412–1416 and 2617–2621 are exceptionally long, spanning over 100 orbits. This extensive length enables us to evaluate the validity of hybridization at an early stage in the binary’s inspiral. The mass ratio for both the SXS:BBH:1412–1416 and 2617–2635 systems falls within the range $1 < q < 10$. As

for the SXS:BBH:2636–2640 systems, the mass ratios are approximately $q \approx 8$. The waveforms SXS:BBH:1412–1416 correspond to spin-aligned systems, while the other systems utilized in our study are precessing systems. The magnitudes of the spin parameters χ_1 and χ_2 are constrained as $|\chi_1|, |\chi_2| \leq 0.8$.

The 8 physical parameters in NR simulations, namely the masses m_1 and m_2 and dimensionless spin vectors χ_1 and χ_2 , are measured quasi-locally on the apparent horizons of the BHs [68]. Therefore, the value of these quantities under this ‘quasi-local’ definition could differ from the PN mass and spin parameters that appear in PN expansions. This difference is accounted for in the matching procedure.

III. MATCHING PN AND NR PARAMETERS

As we will see in Sec. V, the binary parameters used in PN and measured in NR often do not mean the same thing. Therefore, substituting NR parameters for those in the PN expansion will result in an inaccuracy that can cause the differences in the matching window between PN and NR waveforms to be one to three orders of magnitude larger. Therefore, we must identify the proper PN parameters that correspond to the NR systems.

Here we are concerned with optimizing only 12 parameters: 8 PN parameters (q , M , χ_1 and χ_2) and 4 coordinate parameters that determine the SO(3) rotation and time translation. For technical reasons discussed in Sec. IV, we use a different method to determine the additional supertranslation and boost parameters. We will present the complete procedure to determine all the parameters in Sec. IV.

We determine these 12 parameters by minimizing the normalized L^2 difference over a chosen matching window between the fixed NR waveform $h^{\text{NR}}(t)$ and the free PN waveform, $h^{\text{PN}}(t; \vec{\lambda})$, where $\vec{\lambda}$ are the chosen parameters. We define a cost function \mathcal{E} from the normalized L^2 difference between the waveforms,

$$\mathcal{E}[h^{\text{NR}}, h^{\text{PN}}] = \frac{1}{2} \frac{\sum_{\ell, m} \int_{t_1}^{t_2} |h_{\ell m}^{\text{NR}}(t) - h_{\ell m}^{\text{PN}}(t; \vec{\lambda})|^2 dt}{\sum_{\ell, m} \int_{t_1}^{t_2} |h_{\ell m}^{\text{NR}}(t)|^2 dt}. \quad (5)$$

Here t_1 and t_2 are the start and end time of the matching window. \mathcal{E} reduces to sphere-weighted average of the commonly used time-domain mismatch with a flat noise power spectral density (see Appendix C of [69]).

Unless otherwise specified, we typically use a matching window ending at $-8000 M$ for precessing systems, and $-5000 M$ for spin-aligned systems, for the purposes of illustration. We set $t = 0$ at the merger, where the merger is defined as the peak of the L^2 norm of the strain modes.

We use the nonlinear least squares method to perform the minimization.¹ However, it turns out that the cost

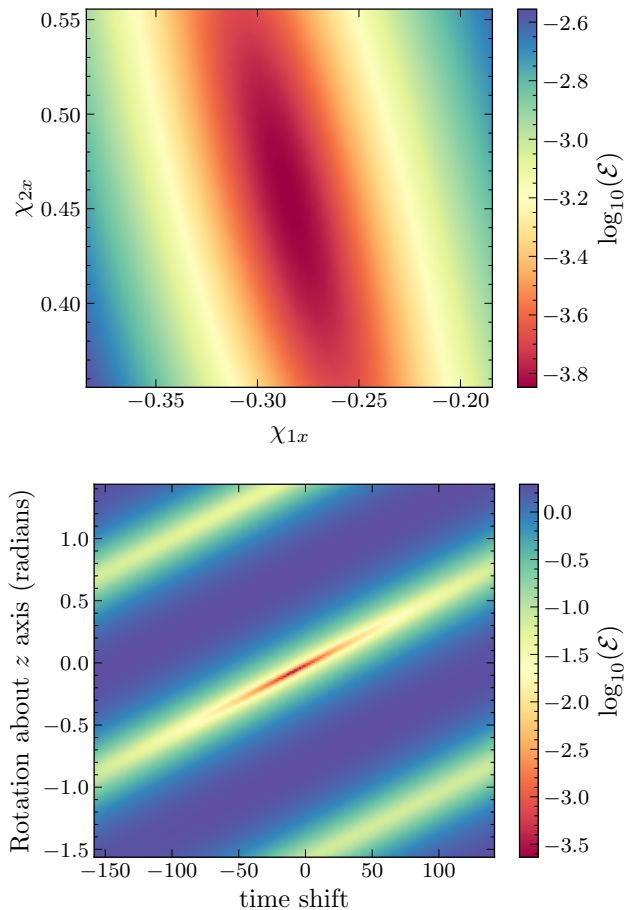


FIG. 2. The profile of the cost function \mathcal{E} with respect to parameters for system SXS:BBH:2617. The matching window is 20 orbits long, and ends 8000 M before merger. In each plot, the 10 other parameters are fixed to their best-fit values. The slanting long and narrow valleys show the degeneracy between these parameters, which can drastically slow down the optimization.

function Eq. (5) has long and narrow valleys that cause the optimizer to run slowly. Fig. 2 shows two examples of the valleys in the cost function. The top plot shows an example of the dependence of the cost function on the x components of χ_1 and χ_2 . We can see that the constraint on χ_1 is better than χ_2 , although they still show some degeneracy between each other. Additionally, the figure on the bottom illustrates the cross section involving the time shift and the z component of the logarithm of the quaternion rotor that rotates the inertial frame. This figure shows the degeneracy between time and phase.

with the Trust Region Reflective algorithm [70, 71]. The tolerances are set to $\text{gtol} = 10^{-8}$ and $\text{xtol}, \text{ftol} = 3 \times 10^{-15}$. We use the NR value of the parameters as the initial guess. The gradient is computed numerically. We impose bounds on the optimization parameters, which we will discuss later in the text.

¹ For the optimization, we use `scipy.optimize.least_squares`

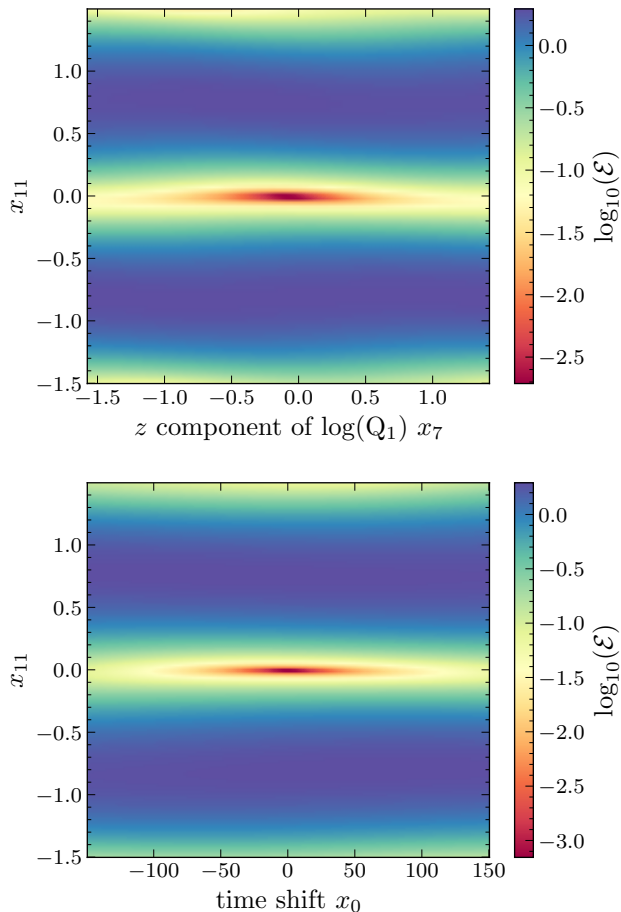


FIG. 3. The profile of the cost function \mathcal{E} with respect to the new parameters for system SXS:BBH:2617. The matching window is 20 orbits long, and ends at $8000M$ before merger. In each plot, the 10 parameters that are not varied are fixed at the best-fit values. These new parameters are no longer degenerate. If the cost function has a narrow diagonal valley, as in Fig. 2, the optimizer tends to zigzag within the valley, leading to a significant slowdown in the optimization process. However, if the valley aligns with an axis, the optimizer can easily re-scale the axis, leading to more efficient optimization.

In order to mitigate these degeneracies and enhance the optimization process, we reparameterize the 12 parameters to diagonalize the valleys. First, we introduce new parameters x_1 to x_4 to describe the fractional change in PN mass ratio q , total mass M , and spin amplitudes compared to their NR counterparts; see Eq. (6). Then, note that the NR value of the spin vectors could be measured in a different Euclidean frame from the PN frame, which is also suggested by the degeneracy between χ_{1x} and χ_{2x} shown in the upper plot of Fig. 2. We therefore introduce the quaternion \mathbf{Q}_1 to describe the rotational transformation of the two spin vectors as a unified entity. This quaternion will have three degrees of freedom, which we parameterize as (x_5, x_6, x_7) . One degree of freedom corresponds to a rotation *about* χ_1^{NR} , and thus has no

effect on χ_1^{NR} itself. But if the two spins are not parallel, that degree of freedom can affect χ_2^{NR} . This leaves just a single degree of freedom representing the rotation of χ_2^{NR} , in a direction orthogonal to both χ_1^{NR} and χ_2^{NR} . This final rotation is encoded as another quaternion \mathbf{Q}_2 that depends on only one additional parameter x_8 . Thus we have

$$\begin{aligned}
 q &= x_1 q^{\text{NR}}, \\
 M &= x_2 M^{\text{NR}}, \\
 \chi_1 &= x_3 \mathbf{Q}_1 \chi_1^{\text{NR}} \bar{\mathbf{Q}}_1, \\
 \chi_2 &= x_4 \mathbf{Q}_2 \mathbf{Q}_1 \chi_2^{\text{NR}} \bar{\mathbf{Q}}_1 \bar{\mathbf{Q}}_2, \\
 \mathbf{Q}_1 &= \exp[(x_5, x_6, x_7)], \\
 \mathbf{Q}_2 &= \exp\left[\frac{x_8}{2} (\widehat{\chi_1^{\text{NR}} \times \chi_2^{\text{NR}}})\right],
 \end{aligned} \tag{6}$$

where the bar represents the conjugate of a quaternion, and the hat over the cross product indicates that the result is normalized. “NR” superscripts denote the NR values of these quantities obtained at the reference time, which we typically set as the end time of the matching window. Here we use the standard quaternion notation, where the exponential of a 3-vector gives a unit quaternion [72].

We also need a quaternion \mathbf{R} , which describes an overall SO(3) rotation of the system,

$$\mathbf{R} = \exp\left[(x_9, x_{10}, x_{11}) + \frac{x_0}{2} \boldsymbol{\Omega}_{\text{tot}}\right]. \tag{7}$$

The $\frac{x_0}{2} \boldsymbol{\Omega}_{\text{tot}}$ term in the quaternion rotor \mathbf{R} is introduced to eliminate the degeneracy between time and phase shown in the bottom plot in Fig. 2. Here x_0 is the parameter that describes the time shift between the NR and PN systems, and $\boldsymbol{\Omega}_{\text{tot}}$ is the total angular velocity measured at the reference time, which captures both orbital and precession contributions. $\boldsymbol{\Omega}_{\text{tot}}$ is measured from the NR strain by defining it as the angular velocity of a rotating frame in which the time dependence of the waveform mode is minimized [72].

When performing the nonlinear least squares optimization, we impose bounds on the parameters defined in Eqs. (6) and (7). For x_{1-4} , the bounds are windows of size $\pm 0.05, \pm 0.02, \pm 0.01$ and ± 0.01 around their respective initial guesses. For x_{5-11} , the range is $\pm \pi/4$, and $\pm 0.5\pi/\Omega_{\text{orb}}$ for the time shift x_0 .

Fig. 3 shows how the new reparameterization can diagonalize the valleys of the cost function and mitigate the degeneracies. This parametrization has been tested on many systems.

We test the optimization routine by using a PN waveform with known parameters as a proxy “NR” waveform, and adjusting the parameters of another PN waveform until the two waveforms match. In most cases, both the original PN parametrization and our new parametrization presented in Eq. (6) and (7) can recover the PN parameters to high accuracy and reduce the waveform differences to $\mathcal{E} \approx 10^{-15}$, as shown in Fig. 4. But for poor initial guesses, our new parametrization generally behaves better than the original PN parametrization, as shown in Fig. 5.

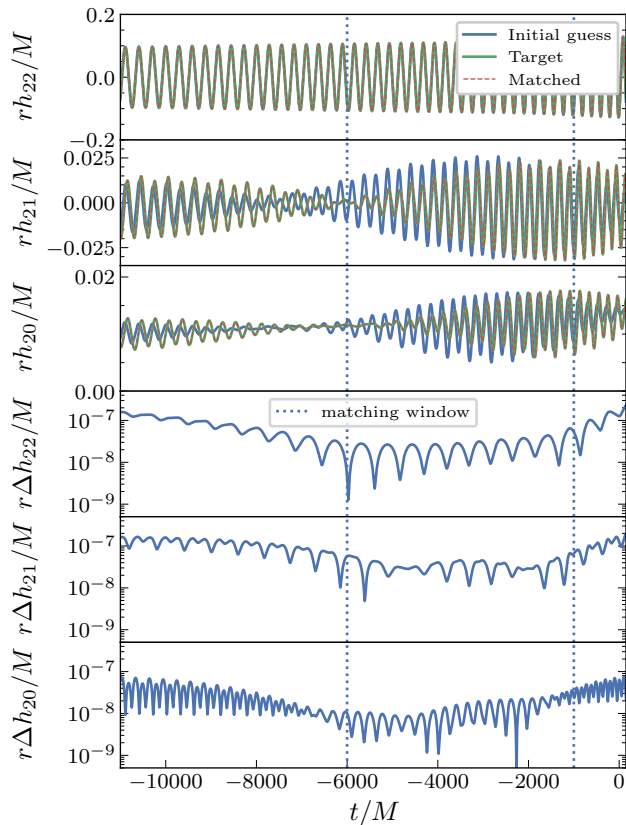


FIG. 4. Strain and residual of two PN waveforms, for a test in which we match the two waveforms by varying the parameters of one of them. The target PN waveform has parameters $q = 1.5$, $M = 1.0$, $\chi_1 = (0.5, 0.2, 0.3)$, $\chi_2 = (0.1, 0.3, 0.4)$, and is rotated away by $\mathbf{R} = \exp(0.05, 0.02, 0.03)$ from the original frame in which the PN waveform is generated. The initial guess is $q = 1.65$, $M = 1.05$, $\chi_1 = (0.42, 0.24, 0.47)$, $\chi_2 = (0.01, 0.20, 0.41)$. The matching window is the region between two vertical dotted lines, which is $5000 M$ long.

IV. HYBRIDIZATION PROCEDURE

In the previous section we described how we determine the PN parameters, the time offset, and the overall rotation of a PN waveform that we match to an NR waveform. However, we also need to account for differences in supertranslations and boosts between the NR and PN waveforms. While it is possible to add extra supertranslation parameters into the cost function defined in the previous section, we find it more efficient to account for all parameters (PN, time shift, boost, rotation, and supertranslations) using the following iterative procedure:

1. Map the NR waveform to its superrest frame, which is defined as the frame in which the Moreschi supermomentum is minimized [31]. The superrest frame is determined during inspiral at the middle of the matching window.

The original CCE waveforms are typically in an ar-

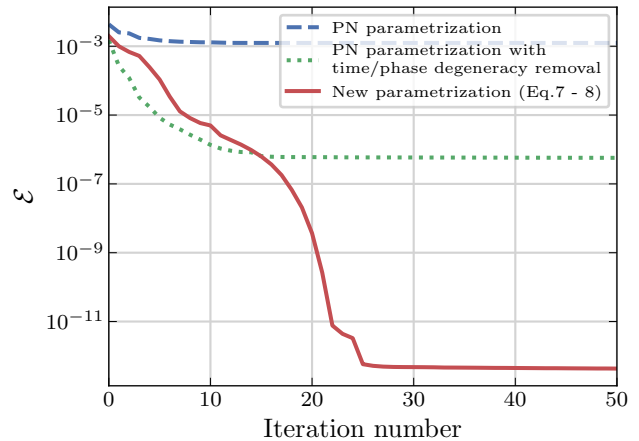


FIG. 5. The convergence of different parametrization methods for a PN-PN matching test, in which we match the two waveforms by varying the parameters of one of them. The target PN waveform has parameters $q = 1.5$, $M = 1.0$, $\chi_1 = (0.5, 0.2, 0.3)$, $\chi_2 = (0.1, 0.3, 0.4)$, and is rotated away by $\mathbf{R} = \exp(0.0, 0.0, 0.05)$ from the original frame in which the PN waveform is generated. The initial guess is $q = 1.65$, $M = 1.05$, $\chi_1 = (0.42, 0.24, 0.47)$, $\chi_2 = (0.01, 0.20, 0.41)$. The matching window is $5000 M$ long. The result using the new parametrization in Eqs. (6) and (7) is shown as the red curve, which converges much faster and better than the original PN parametrization, which is shown as the blue dashed curve. The green dotted curve also uses the original PN parametrization but incorporates the $\frac{x_0}{2}\mathbf{\Omega}_{\text{tot}}$ term in the frame rotor \mathbf{R} defined in Eq. (7). In other words, it uses $(x_0, q, M, \chi_1$ and $\chi_2)$ and $(x_9$ through $x_{11})$ as parameters. The green dotted curve shows better convergence than the blue dashed curve.

bitrary BMS frame with large center-of-mass charge and supermomentum, resulting in significant oscillations in the strain mode amplitudes and orbital frequency. These irregularities introduce bias when determining the PN parameters. Mapping the NR waveform to its superrest frame reduces the effects caused by a large center-of-mass charge and supermomentum, mitigating biases and enabling a more accurate optimization of the PN parameters.

2. Set the $m = 0$ modes of the NR and PN waveforms to zero in their corotating frame.

The $m = 0$ modes have the most memory contribution, and are thus more influenced by the supertranslations involved in the BMS frame transformation. Since the superrest frame of the NR system differs from the PN BMS frame, the strain modes in these two frames are expected to differ as well. This can also introduce bias when optimizing PN parameters. Therefore, we set $m = 0$ modes to zero in their corotating frame to exclude the principal memory contributions to the strain. Note that the $m = 0$ modes will be restored in step 4 and the steps thereafter.

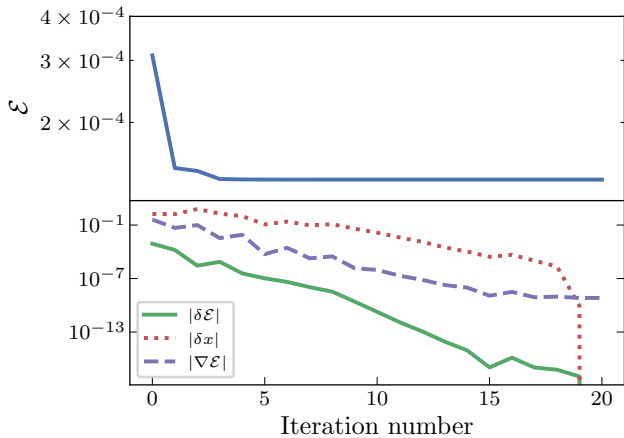


FIG. 6. The convergence of the 12-D nonlinear least-squares optimization for system SXS:BBH:2617 in the second iteration of step 6 of the procedure in Section IV, using the parameters from the first iteration as the initial guess. The horizontal axis is the iteration number for the 12-D optimization. The end of the matching window is $5000 M$ before merger, and is 20 orbits long. The blue curve shows the value of the cost function, and the green solid and red dotted curves show the reduction of the function value and the norm of change in parameters after each iteration. The norm of the gradient of the cost function is shown in dashed purple.

3. Perform the 12D optimization described in the previous section to determine the 8 PN parameters, rotation, and time shift.
4. Now with the $m = 0$ modes of the original NR waveform included, map the original NR waveform to the BMS frame of the resulting PN system by applying the supertranslations that map the NR Moreschi supermomentum to the PN Moreschi supermomentum, and also applying the boost that minimizes the center-of-mass charge. Note that the PN Moreschi supermomentum depends on the PN parameters, so the NR waveform obtained by this step depends on the current values of the PN parameters.
5. Again perform the 12D optimization, but using the NR waveform from step 4, including the $m = 0$ modes in the PN waveform.
6. Iterate steps 4 and 5 until the relative change in \mathcal{E} is less than 10^{-2} .
7. Use a smooth stitching function to hybridize the PN and NR waveforms over the matching window.

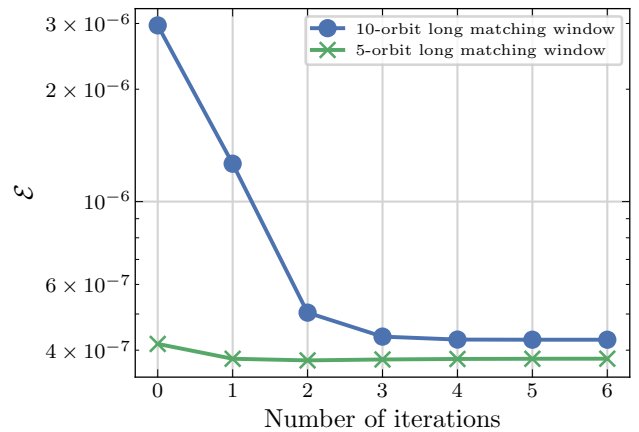


FIG. 7. The convergence of iterations of step 6 of the procedure in Section IV for system SXS:BBH:1414. The 0th iteration is step 3 of the procedure in section IV, for which the NR waveform is mapped into the superrest frame, and for this iteration the error does not include the $m = 0$ modes since the value of the strain in these modes in the superrest frame does not agree with PN. For the other iterations, the NR waveform is mapped to the PN BMS frame, and the errors include the $\ell \leq 8$ modes. The blue curve uses a 10-orbit long matching window that ends $8000 M$ before merger, and the green curve uses a 5-orbit long matching window that ends $2000 M$ before merger. Both curves converge within 4 iterations. The cost function for the shorter matching window is smaller and converges less rapidly than the case with a longer matching window, likely because the short waveforms are being overfit. This overfitting is explored in Sec. VII C.

Our stitching function is the smooth transition function

$$\tau(t) = \begin{cases} 0 & t < t_1, \\ \left\{ 1 + \exp \left[(t_2 - t_1) \left(\frac{1}{t-t_1} + \frac{1}{t-t_2} \right) \right] \right\}^{-1} & t_1 \leq t \leq t_2, \\ 1 & t_2 < t. \end{cases} \quad (8)$$

The hybridized waveform is then

$$h_{\ell m}^{\text{Hyb}}(t) = [1 - \tau(t)]h_{\ell m}^{\text{PN}}(t) + \tau(t)h_{\ell m}^{\text{NR}}(t), \quad (9)$$

where h^{PN} is the PN waveform obtained with the given x_i parameters and $h_{\text{BMS}}^{\text{NR}}$ is the NR waveform in the adjusted BMS frame, as obtained in step 4 of the iterative procedure.

The convergence of the 12-D optimization is tested for the NR-PN hybridization case with comparable BH masses, as shown in Fig. 6. The optimization typically converges within tens of iterations.

The process of iteratively optimizing PN parameters and mapping the NR waveform to the resulting PN BMS frame demonstrates rapid convergence for cases with comparable BH masses, as illustrated in Fig. 7. In the case of

shorter matching windows, the decrease in the cost function during each iteration is less pronounced compared to longer matching windows. This can be attributed to the limited information contained within shorter windows, which may result in overfitting. We will further address this problem in Sec. VII C. The iteration process typically converges within 2–4 steps.

For cases with a larger mass ratio ($q \sim 8$), larger eccentricity ($e > 0.05$), or larger χ_p (> 0.5), both the 12-D optimization and the overall iterative procedure converge more slowly. For these cases, the 12-D optimization typically takes more than a hundred iterations, and the overall iterative procedure typically takes more than 10 iterations. This slowdown occurs because for systems with large mass ratios, the waveforms become less sensitive to the smaller black hole’s properties. And for systems with larger χ_p or eccentricity, the PN and NR waveforms that we use become intrinsically different, as we will show in Sec. VI. These features make the optimization more challenging.

V. RESULTS

A. Comparison between PN and NR waveforms

We present typical hybridization results for spin-aligned systems and precessing systems in Figs. 8 and 9. For the early inspiral stage, the PN and NR waveforms agree quite well, up to the systematic errors (eg., non-zero eccentricity of NR systems, absence of PN terms, etc.) that we will discuss in Sec. VI.

Apart from systematic errors in the early inspiral stage, we notice the PN failure thousands of M before merger as the differences between the NR and PN strain modes become much larger. We will be interested in the frequency at which the PN truncation error becomes larger than other systematic errors that affect our hybridization procedure. Later we will choose the matching window to end before this frequency, so that the PN truncation error has a negligible effect on the matching procedure compared to the other errors.

The PN expansion parameter is $v = (M\Omega_{\text{orb}})^{1/3}$, and each power of v counts for $\frac{1}{2}$ PN order. PN waveforms that are complete up to N PN order have truncation errors at relative order $\mathcal{O}\left(\Omega_{\text{orb}}^{(2N+1)/3}\right)$. Therefore, the frequency at which PN truncation error becomes dominant satisfies

$$\left(\text{Coefficient} \cdot \Omega_{\text{orb}}^{(2N+1)/3}\right)^2 \approx \mathcal{E}_{\text{sys}}, \quad (10)$$

where \mathcal{E}_{sys} is the norm of differences induced by other systematic errors. The systematic errors include errors that can cause the differences between NR and PN beyond PN truncation. These may arise from numerical errors, eccentricities in NR binaries that are meant to be quasircular, inaccuracies in PN parameters, imprecise BMS frame alignment, incomplete consideration of certain physical aspects in PN or NR models like high order spin

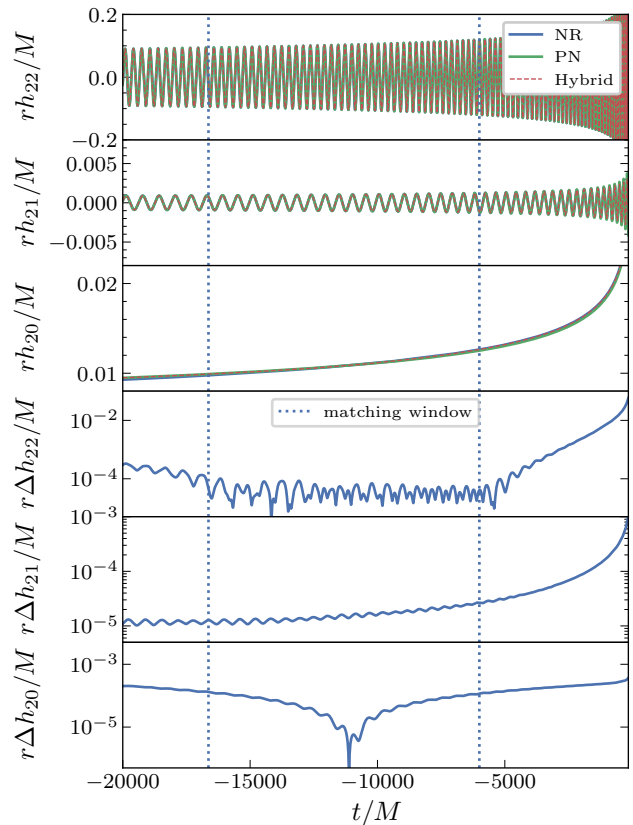


FIG. 8. Strain and residual of the hybridized spin-aligned system SXS:BBH:1412. The matching window is the region between the two vertical dotted lines, which is 20 orbits long and ends at $-6000 M$. The blue, green and red curves in the upper panel are the strain modes of the NR, PN and hybrid waveforms. The blue curves in the lower panel are the residuals between the NR and PN strain modes.

interactions in PN, or inaccurate boundary conditions in NR, and more. We will explore further the systematic errors that limit our hybridization accuracy in Sec. VI.

B. Improvement from PN parameters and BMS frame fixing

In Figure 10, we present the hybridization errors of 29 systems. The hybridization error plotted is the cost function in Eq. (5) computed within a 10-orbit matching window. However, only the brown markers in the figure represent errors computed using the full hybridization procedure described in Section IV. The other markers represent results obtained using only parts of the procedure, omitting some of the waveform modes, or using NR waveforms that are not obtained using CCE; these markers are included to illustrate the need for all parts of the procedure described in Section IV. For all the markers, the 4 parameters representing the 3D rotation and time shift between the PN and NR waveforms are optimized

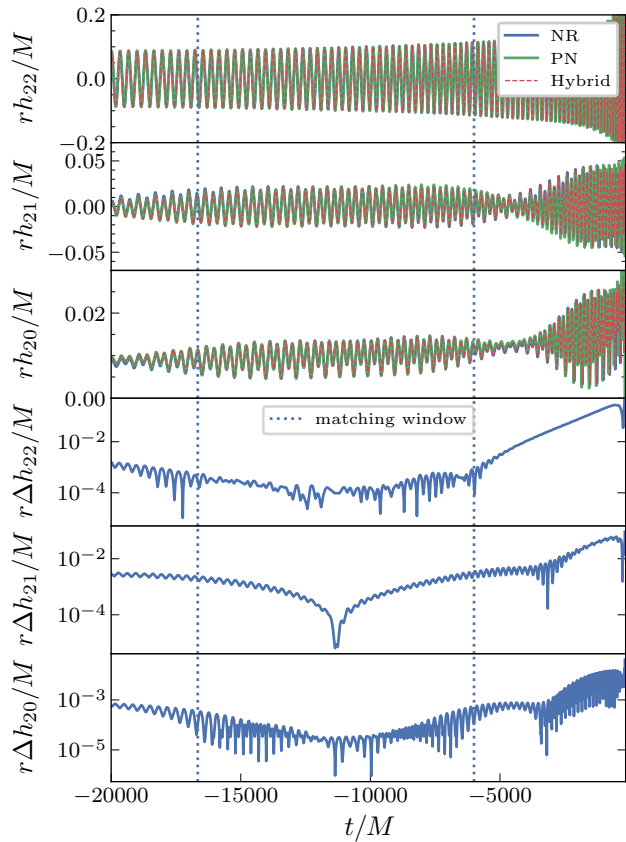


FIG. 9. Strain and residual of the hybridized precessing system SXS:BBH:2619. The matching window is the region between the two vertical dotted lines, which is 20 orbits long and ends at $-6000 M$. The blue, green and red curves in the upper panel are the strain modes of the NR, PN and hybrid waveforms. The blue curves in the lower panel are the residuals between the NR and PN strain modes.

to obtain a minimal hybridization error. The triangular markers use extrapolated NR waveforms obtained using the methods described in [42], which lack the correct memory effect. The circular markers use CCE waveforms that include memory contributions and contain enough information to allow suitable BMS transformations. The blue triangular markers denote errors obtained from the extrapolated waveforms without adding supertranslations, and with the 8 PN parameters fixed to their corresponding NR values. The extrapolated waveforms get a different CoM-correction that is described in [73]. Because the extrapolated waveforms lack the correct memory terms, we include the green triangular markers, which are obtained by setting the $m = 0$ modes to zero in the NR corotating frame before hybridization, and then plotting the hybridization error of only the $m \neq 0$ modes. For the green triangular markers, the PN parameters are fixed to their corresponding NR values. The errors represented by the pink, purple, and brown circular markers include all modes including $m = 0$. The pink circular markers utilize

CCE waveforms, but the NR waveforms are in their inspiral superrest frames, and the PN parameters are fixed to their corresponding NR values at the reference time. The purple circular markers map the NR waveforms to the corresponding PN BMS frame, but the PN parameters used in both the PN waveform and to define the PN BMS frame are the corresponding NR values of those parameters. Comparing the pink and purple circular markers, we observe that by fixing the BMS frame we can improve the error between PN and NR waveforms by 1 to 3 orders of magnitude. This indicates that CCE NR waveforms are usually in a BMS frame that differs from the PN BMS frame, and aligning the BMS frame is crucial when comparing or hybridizing two GW waveforms.

By optimizing PN parameters in addition to optimizing time shift and rotation, as shown in the red and brown, we further reduce \mathcal{E} by 2 to 3 orders of magnitude for spin-aligned systems and up to 3 orders of magnitude for precessing systems. This suggests that the NR parameters at the reference time are different from the parameters that yield the best-matching PN waveform. Figure 11 shows the difference in parameters for selected systems, using the full hybridization procedure described in Section IV, which corresponds to the brown markers in Fig. 10. We see that the difference in mass ratio q between PN and NR is around 10^{-2} , the difference in total mass M is around $10^{-3} \sim 10^{-2}$, and the difference in spin magnitudes is around $10^{-2} \sim 10^{-1}$.

Given that the best-fit PN parameters can be significantly different from the NR parameters in some cases, it is possible that the optimization over intrinsic PN parameters leads to overfitting. Missing PN terms or NR truncation errors can potentially be absorbed by this optimization, leading to an incorrect PN waveform getting attached to the NR waveform. While Figure 10 does not capture this effect because it only shows the errors in the matching window, one can check this by comparing the errors between PN and NR in an earlier test window that was not included in the optimization. This will be done in Sec. VII.

VI. SOURCES OF ERROR

In this section, we study the origin of the hybridization error. We have two goals in mind: first, we would like to better understand how to improve the hybridization procedure using current NR waveforms and currently known PN terms. Second, we would like to know whether the hybridization error is at present limited by our current NR waveforms or our knowledge of PN, so that we can understand what is needed in terms of NR or PN improvements to reduce hybridization errors in the future.

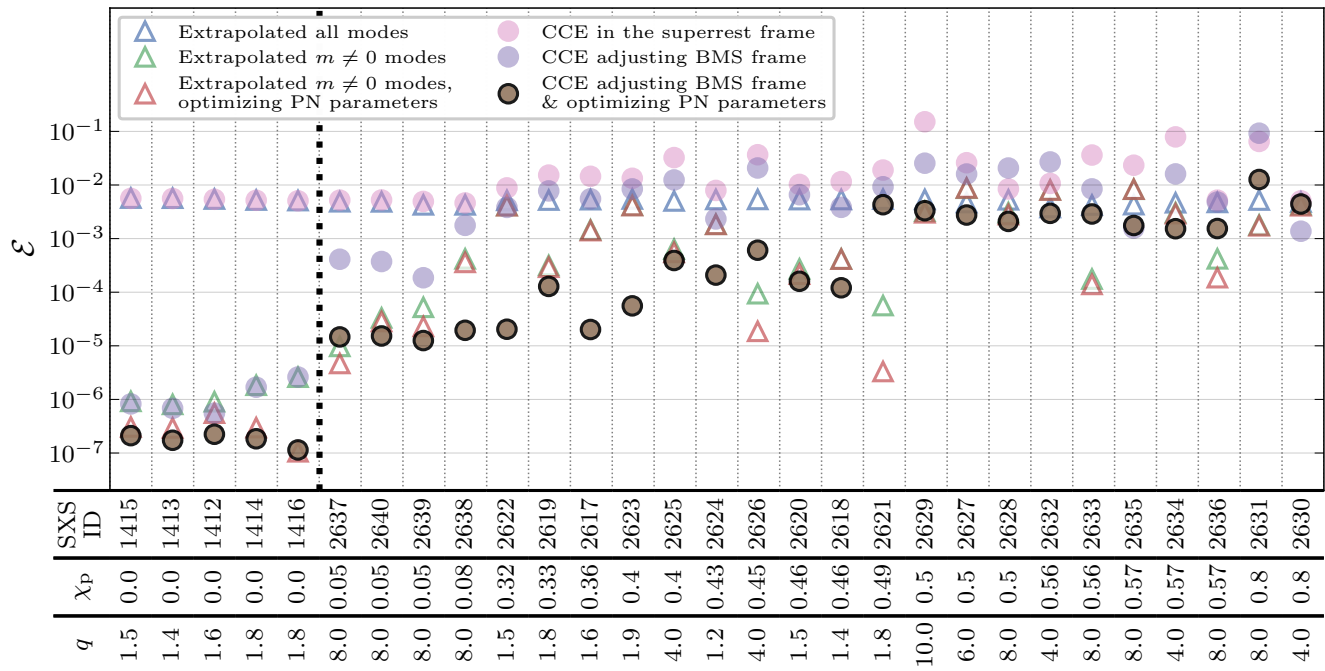


FIG. 10. Hybridization errors in the matching window, Eq. (5), for different waveforms and for different methods of choosing PN parameters and matching the BMS frame. See text for details. All the errors are measured after adjusting the 3-D rotation and time shift. The BMS frame for extrapolated waveforms cannot be modified using the method described in this paper because those waveforms do not have an accurate value of Ψ_2 to calculate the Moreschi supermomentum. We only adjust the BMS frame for CCE waveforms. Systems on the left of the vertical dotted line are spin-aligned systems; systems on the right are precessing systems, and systems are ordered left to right by χ_p . The mass ratios for SXS:BBH:2617–2635 systems are $1 < q < 10$ and for SXS:BBH:2636–2640 systems are $q \approx 8$. The matching window is 10 orbits. For systems other than the SXS:BBH:2636–2640 systems, the matching window ends 8000 M before merger. For the SXS:BBH:2636–2640 systems the matching window ends 5000 M before merger because these systems are not long enough. The brown markers use the full hybridization procedure described in Section IV.

A. Spin-aligned systems

For spin-aligned systems, we can see from Fig. 10 and Fig. 12 that the error inside the matching window is on the order of 10^{-7} .

The blue curve in Fig. 12 shows \mathcal{E} in a 15-orbit long matching window with a varying end time, and it has a local minimum when the angular velocity is around 0.012, or between 3000–8000 M before merger. The increase in hybridization error after the minimum, where the end time of the matching window gets closer to merger, corresponds to the expected late-time PN failure that we discussed in Sec. V A. We will show below that the increase in hybridization error before the minimum, where the matching window is moved earlier and thus farther from merger, is consistent with the effects of using an NR waveform with small but nonzero orbital eccentricity to hybridize with a PN waveform that assumes eccentricity is identically zero. The green curve in Fig. 12 will be discussed later in Sec. VI A.

The contribution of eccentricity to the leading order in

PN quasi-Keplerian expansion is given by [75]

$$h_{\text{Newt}}^{22} \propto 1 + e \left(\frac{1}{4} \exp(-i\xi) + \frac{5}{4} \exp(i\xi) \right), \quad (11)$$

where e is the time-evolving eccentricity parameter. The angle ξ is closely related to the mean anomaly, going through roughly 2π with each orbit. From Eq. (11) we can obtain the PN prediction of the L^2 normalized difference \mathcal{E}_{sys} between eccentric PN waveforms and non-eccentric PN waveforms in the limit of small eccentricity as

$$\mathcal{E}_{\text{sys}} \propto e^2. \quad (12)$$

In Fig. 13 we plot \mathcal{E} between PN and NR for 10 different systems. The error increases with the eccentricity, and is roughly consistent with the expected $\mathcal{E} \propto e^2$ behavior of Eq. (11).

In addition to examining the overall magnitude of \mathcal{E} caused by eccentricity, we also examine the time evolution of eccentricity and its effect on \mathcal{E} . The time evolution of eccentricity to leading order is given by [76]

$$e_t(\Omega_t) \approx e_0 \left(\frac{\Omega_0}{\Omega_t} \right)^{19/18}, \quad (13)$$

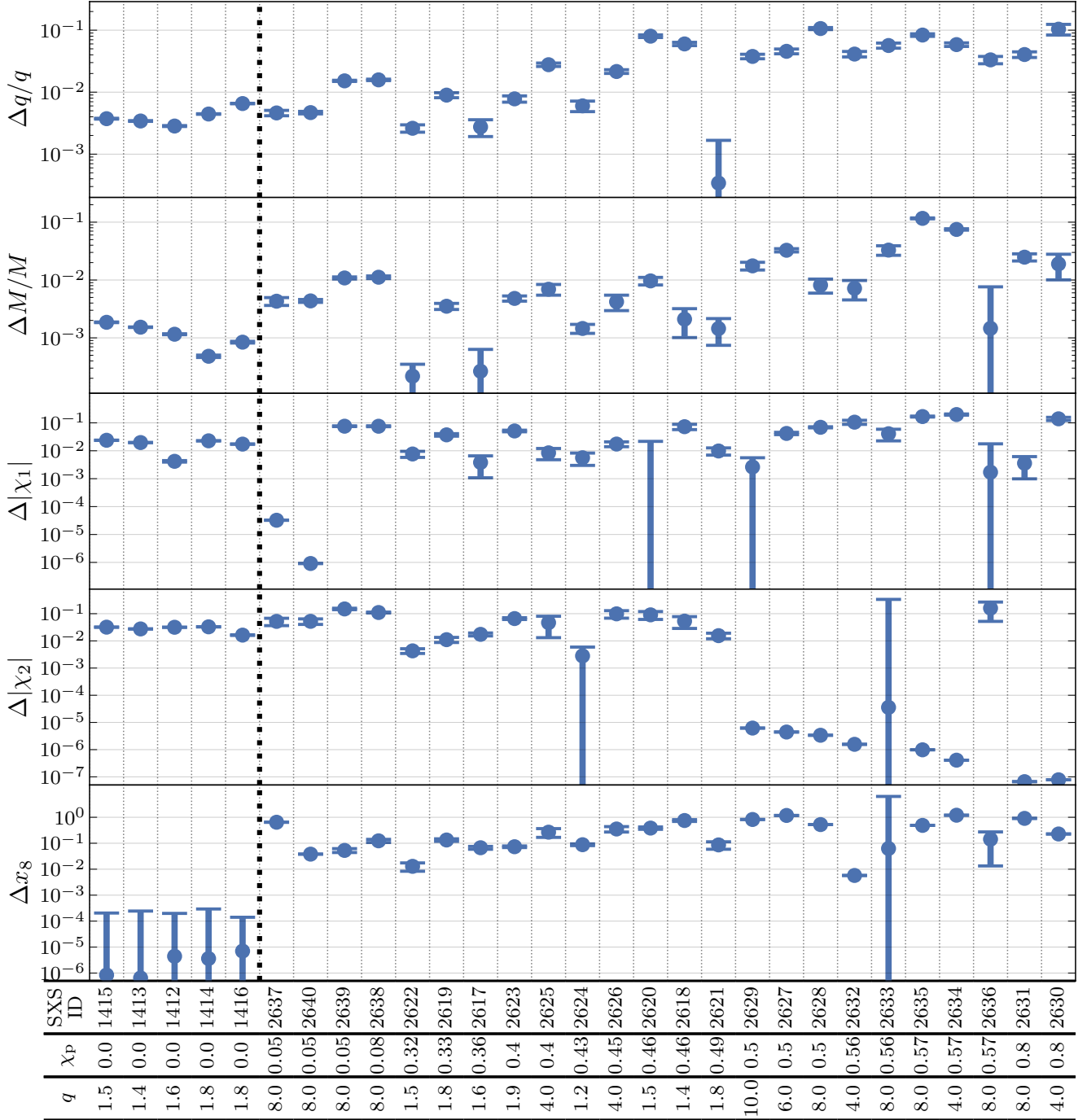


FIG. 11. The differences in parameters between NR and PN for selected waveforms hybridized using the procedure of Section IV. Plotted ΔX is $|X_{\text{NR}} - X_{\text{PN}}|$ for selected parameters X . Systems on the left of the vertical dotted line are spin-aligned systems; systems on the right are precessing systems, and systems are ordered left to right by χ_p . The mass ratio for SXS:BBH:2617–2635 systems are $1 < q < 10$, for SXS:BBH:2636–2640 systems are $q \approx 8$. The error bars show the uncertainties of the optimization, and the markers show the best-fit value of the parameters.

where Ω_t is the orbital frequency at time t , and Ω_0 is the orbital frequency at a fiducial time when the eccentricity is e_0 . According to Eqs. (11) and (12), the oscillation amplitude of the norm of the $(2, 2)$ mode should be proportional

to $e \propto \Omega^{-19/18}$. We check the oscillation amplitude of the norms of the $(2, 2)$, $(2, -2)$, $(2, 1)$ and $(2, -1)$ modes for system SXS:BBH:1412. The oscillation amplitude is obtained by subtracting the individual mode's norm

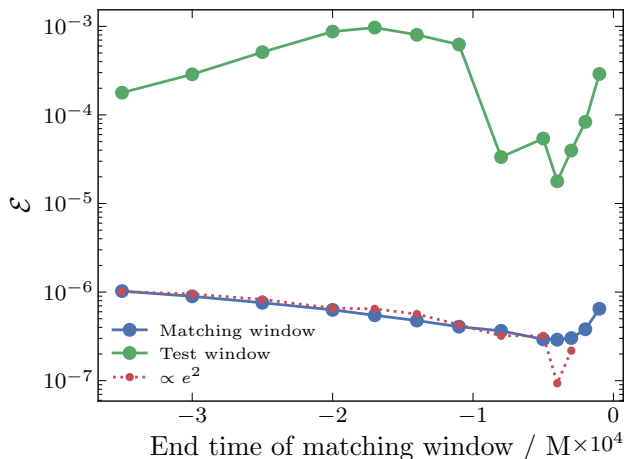


FIG. 12. Hybridization error for different locations of the matching window for system SXS:BBH:1412. We vary the end time of the matching window, while keeping the matching window 15 orbits long. The test window is 10 orbits long, and the center (in number of orbits) of the test window is 30 orbits earlier than the center of the matching window. The red dotted curve shows the square of the eccentricity measured using `gw_eccentricity` [74] by the amplitude fitting method at the middle of the matching window multiplied by a factor of 15. The factor is obtained by varying the overall amplitude of the red curve until it overlays the blue curve.

from its orbital average, which is obtained by applying a low-pass filter to the original mode. We find that the oscillation amplitudes of the norms of the above modes are proportional to $\Omega^{-19/18}$ and are thus consistent with eccentricity damping. The same argument applies to \mathcal{E} within the matching window as we show in Fig. 12. Assuming that the change of e and Ω in the window is small, then $\mathcal{E} \propto e^2 \propto \Omega^{-19/9}$. The red dotted line is e^2 scaled by a coefficient found by varying the overall amplitude of the green curve until it overlays the blue curve, where the eccentricity e is measured from the waveform amplitude fit of the $(2, 2)$ mode using the package `gw_eccentricity` [74], and measurements are taken at the middle of the different matching windows. The blue curve, which is \mathcal{E} between PN and NR, agrees very well with the green curve, which shows the expected effect of eccentricity damping.

We also remark, based on Eq. (11), that the eccentricity contribution oscillates at the same frequency as the orbital frequency, and is symmetric for positive and negative m . We therefore check the oscillation amplitudes of the norms of the $(2, 2)$ and $(2, -2)$ modes for a system with a greater eccentricity, SXS:BBH:1168. The oscillation amplitudes and phase for these two modes are indeed the same, which is consistent with the above arguments for eccentricity.

On the basis of these arguments, one might assume that the hybridization error would be reduced if we included eccentricity and mean anomaly in our PN parameter optimization. However, by conducting such a 14-dimensional

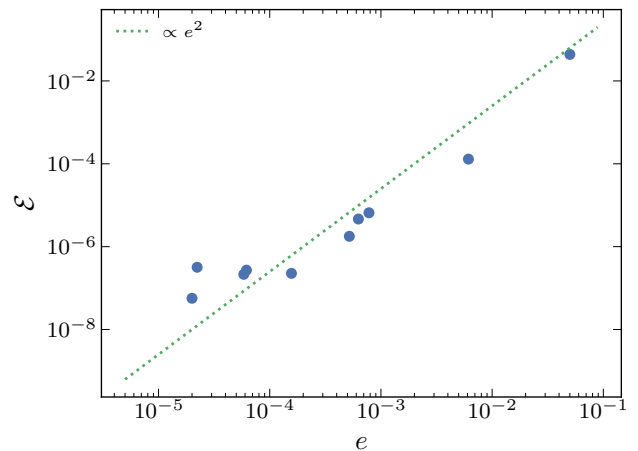


FIG. 13. The L^2 normalized error \mathcal{E} versus eccentricity e for 10 different systems: SXS:BBH:1412–1416, SXS:BBH:1153, 1164, 1165, 1168 and 3618. The end time of the matching window is $-5000 M$, and the length of the matching window is 10 orbits. The green dotted curve is a quadratic fit to the plotted points.

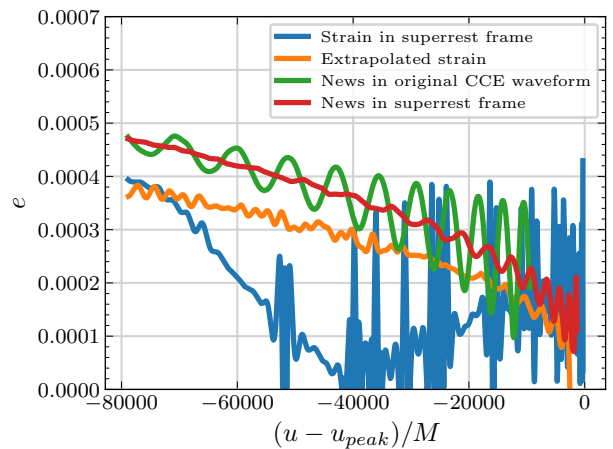


FIG. 14. Measurement of eccentricity e from both strain and news (the time derivative of strain), and in different BMS frames, for system SXS:BBH:1412. When transforming to a superrest frame, the frame is determined from the middle of the inspiral.

optimization in the superrest frame of the NR system, we found that the error couldn't be reduced further since the error generated by such a small eccentricity is overpowered by the error caused by the incorrect BMS frame. Fixing the BMS frame, however, is not a simple task when eccentricity is present, as both eccentricity and supertranslation can produce oscillations in the waveform mode amplitudes and the angular velocity. This degeneracy is depicted in Fig. 14, where we plot the eccentricity measurement in different BMS frames as a function of time. We can see by comparing the blue and orange lines

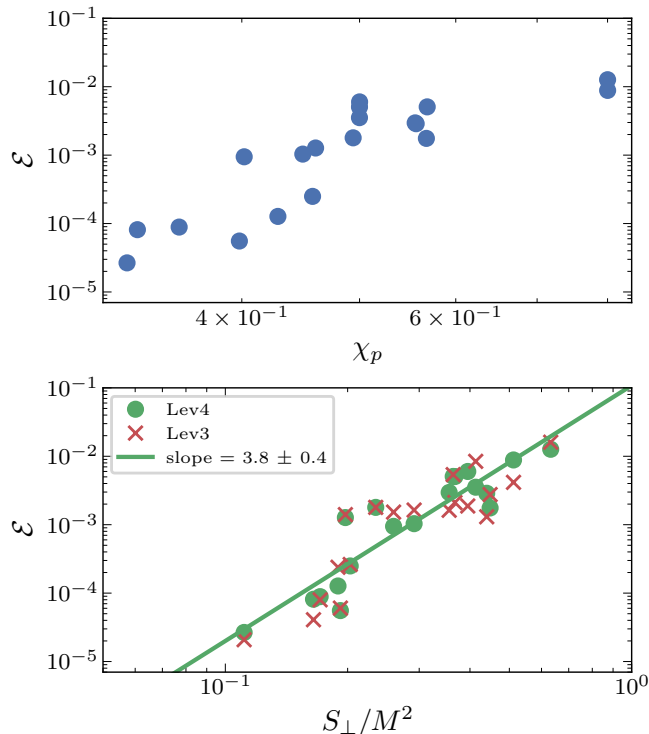


FIG. 15. Hybridization error, Eq. (5), inside the matching window for precessing systems SXS:BBH:2617–2635. The horizontal axis is the spin-precession parameter χ_p for the upper panel, and S_{\perp}/M^2 for the lower panel. Here $\mathbf{S}_i = \chi_i m_i^2$ is the spin angular momentum, and S_{\perp} is the magnitude of the projection in the orbital plane. Results are shown for two different choices of the resolution parameter “Lev” used to compute the NR simulation. Lev4 uses a finer tolerance for the adaptive-mesh-refinement algorithm than Lev3, so Lev4 has smaller numerical errors. The matching window is 10 orbits long, and the end time is 8000 M before merger.

that the measurement of eccentricity from the strain has strong dependence on the method of obtaining the asymptotic waveform. The measurement of eccentricity from the Bondi news—the time derivative of the strain—is less dependent on the BMS frame, but there are still large oscillations with respect to the measurement time. Because of the degeneracy between supertranslations and eccentricity, including eccentricity in hybridization is nontrivial and we leave it for future work.

B. Precessing systems

In Figure 15, we present the hybridization errors within the matching window for various precessing systems. The horizontal axis for the upper panel is the spin-precession parameter χ_p . Notably, these blue dots reveal a correlation between the hybridization error and the spin precession for each system.

To discern whether the error is caused by the numer-

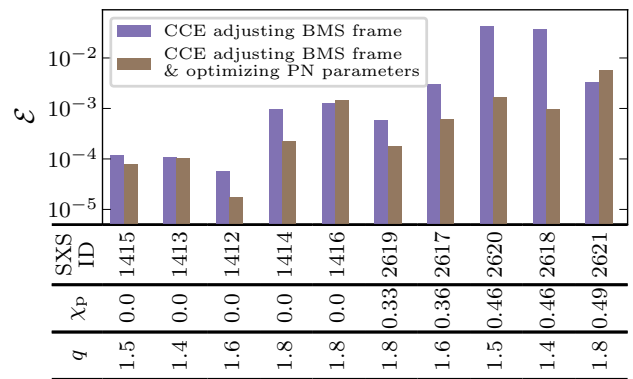


FIG. 16. Test window error for 10 long waveforms from Fig. 10. The center of the test window is 30 orbits earlier than the center of the matching window. The matching window is the same with Fig. 10. For most systems, the optimization over PN parameters can result in smaller error in both the matching window and the test window.

ical error of NR spin-precession or the absence of spin-precession terms in PN, it is important to recognize that the spin terms entering the PN expansion are the spin angular momentum $\mathbf{S}_i = \chi_i m_i^2$, rather than χ_p . To investigate this, in the lower panel we plot the hybridization error for the same systems against $S_{\perp}/M^2 = (S_{1\perp} + S_{2\perp})/M^2$ using two different NR simulations that are identical except for the resolution parameter “Lev” that determines the error tolerance of the simulation. Larger “Lev” means a smaller error tolerance, which translates into a more accurate (but more computationally expensive) NR simulation. By comparing the green dots and red crosses, it is evident that the NR numerical error is not the limiting error source. The slope of the green dots is 3.8, implying that the slope of the absolute difference between PN and NR waveforms should be 1.9. Note that the contribution of the missing PN precession-dependent spin-spin terms to the waveform is expected to be proportional to $(S_{\perp}/M^2)^2$, so our result is consistent with those missing terms being the dominant source of error.

VII. CHOICE OF MATCHING WINDOW

The matching window should be selected so that both PN and NR are valid there and agree with each other to an acceptable tolerance. We can estimate the matching window’s end time by Eq. (10), which estimates the frequency at which PN becomes inaccurate at late times: When the left-hand side of this equation exceeds the right-hand side, the PN truncation error becomes dominant in the hybridization error, and this error grows polynomially with the orbital frequency as we get closer to merger. If the matching window is chosen earlier so that the left-hand side is smaller than the right-hand side, the hybridization error is then dominated by the remaining systematic

errors that we are not able to eliminate for now.

However, Eq. (10) typically has undetermined coefficients, which depend on parameters of the system. In addition, Eq. (10) does not tell us how to determine the *length* of the matching window. In sections VII A and VII B below, we will describe our method of choosing the matching window, which is different for spin-aligned and precessing systems.

Recall that the hybridization method involves varying the PN parameters and frame parameters to minimize the PN-NR differences in the matching window. It is not appropriate to simply compare PN to NR in the window where the difference is optimized. To better evaluate how well we match PN and NR, we also compare PN-NR differences in a new window, called a *test window*, that is outside the matching window so that PN-NR differences are not minimized there, and that is earlier in time than the matching window so that both PN and NR should be valid there. The idea is that for a good choice of matching window, and for sufficiently accurate NR and PN waveforms, the PN-NR differences in the test window should also be small. Unless otherwise specified, the test window is chosen to be 10 orbits long, and the center of the test window (in number of orbits) is 30 orbits earlier than the center of the matching window.

We also show the test window error for 10 long waveforms in Fig. 16. By comparing the brown and the purple columns, we can see that for most systems, the optimization over PN parameters can result in smaller error in the test window.

A. Spin-aligned systems

Figure 12 shows how we determine the end time of the matching window for spin-aligned systems. In this figure, we fix the length of the matching window as 15 orbits long, and vary the end time of the matching window. We plot \mathcal{E} in both the matching window and the test window as blue and green curves, respectively. We can see that there is an optimal choice for the end time of the matching window, which is about $3000 M$ to $8000 M$ before merger, where the errors in the matching and test windows show a minimum. For matching windows ending earlier than this optimum, the errors are larger because of larger eccentricity, as shown in Sec. VI. The slope of the blue curve before $-5000 M$ agrees very well with eccentricity damping, which is shown as the red dotted curve. For matching windows ending later than the optimum, we get larger errors because PN breaks down at late times.

The other free parameter is the matching window’s length. Generally speaking, the matching window should be as long as possible, provided that the numerical error of the NR waveform is less than the systematic error stated in Sec. VI. However, most current NR simulations are short, and long NR simulations are very expensive. If the NR waveform is too short to include sufficient data, the hybridization model will be invalid.

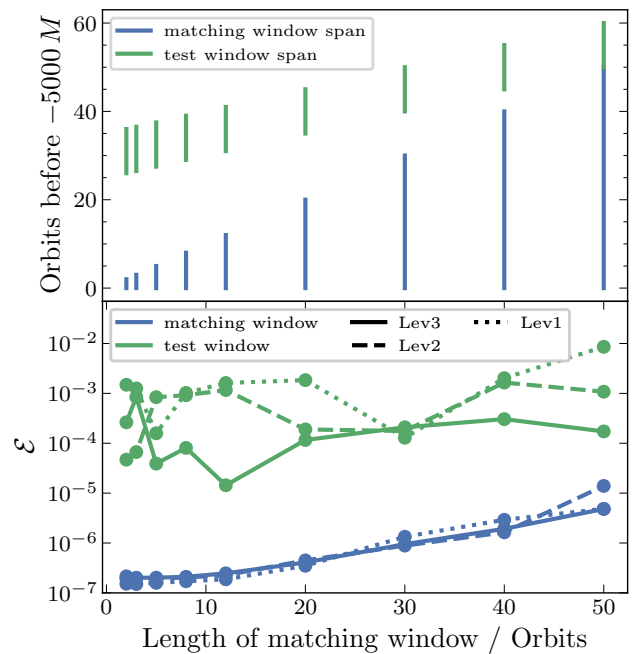


FIG. 17. The hybridization error for different lengths of matching window for spin-aligned system SXS:BBH:1412. We fix the end time of the matching window to be $5000 M$ before merger. The test window is 10 orbits long, and the center of the test window (in number of orbits) is 30 orbits earlier than the center of the matching window. “Lev” labels the resolution of the NR simulations, as in Fig. 15.

To find the minimal duration of the matching window, we fix the end time based on Figure 12, and change the start time. We also use a test window to check the results. The position of the matching window and test window are shown in the upper panel of Fig. 17, and the hybridization errors in both windows are shown in the lower panel. The solid, dashed, and dotted curves in the lower panel show the errors using NR waveforms with different numerical resolution, labeled by “Lev” as in Section VI above. We can see from the blue curves that the NR numerical error does not significantly affect the hybridization error in the matching window. But when comparing the green curves, we can see that the errors in the test window roughly converge to smaller values as we increase the resolution. This suggests that low-resolution NR simulations can accumulate numerical phase error over long periods of time.

We can see from the solid green and blue curves that the optimal length of matching window should be around 5 to 20 orbits. The shorter the matching window is, the less information it includes, and the larger the chance that the small error in the matching window is spurious; for very short matching windows (< 5 orbits) the green curves no longer converge and the solid green curve shows a large error in the test window. For longer matching windows (> 20 orbits), the green solid curve becomes

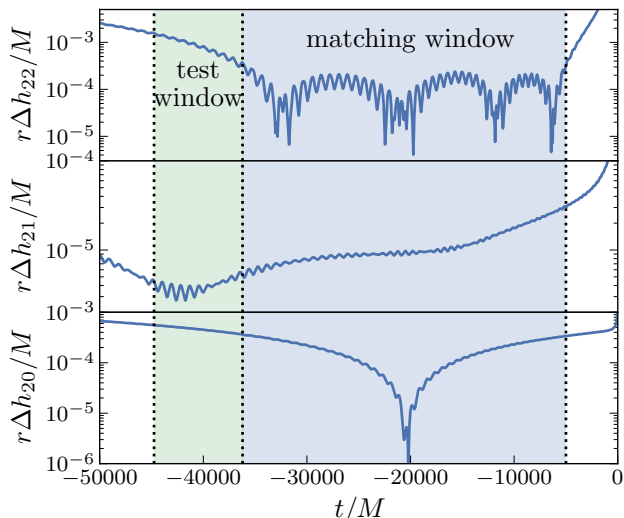


FIG. 18. The residual of spin-aligned system SXS:BBH:1412 corresponding to the rightmost points for Lev3 in Fig. 17. The matching window is 50 orbits long and ends at $5000 M$ before merger, and the test window is 10 orbits long and immediately before the matching window. The error increases rapidly outside the matching window, so that the error in the test window is much larger than the error in the matching window. The error increases outside the matching window because of slight differences between the PN and NR waveforms. In this spin-aligned case, we use non-eccentric PN to hybridize with a slightly eccentric NR waveform. While we can minimize the error within the matching window, the inherent differences between the models prevent us from reducing the error outside.

flat and the blue curves increase. This is because on the one hand, the start time of the matching window is earlier, where the NR eccentricity is larger, resulting in a larger error in the matching window, as shown by the blue curve in Fig. 12. On the other hand, a longer matching window leads to more accumulated phase error, potentially caused by both the disagreement between zero-eccentricity PN and small-but-finite-eccentricity NR, as well as insufficient NR resolution. In Fig. 18, we plot the residual corresponding to the rightmost points for Lev3 in Fig. 17. We can see that even if the matching window is long enough to be adjacent to the test window, we still cannot achieve good alignment between PN and NR outside the matching window. The error increases beyond the matching window because the PN and NR waveforms are inherently not identical. In this case of spin-aligned systems, we use a non-eccentric PN model to hybridize with NR waveforms that possess slight eccentricity. Given the inherent differences between the waveform models, it is not possible to reduce the error outside the matching window, even if we achieve minimal error within it.

For NR waveforms with different and small but nonzero eccentricities, the best location of the matching window could be slightly different. We can refer to Eq. (10) and Eq. (12). Error due to non-zero eccentricity and error

from breakdown of PN are comparable when

$$\text{Coefficient} \cdot e^2 \approx \left(\text{Coefficient} \cdot \Omega_{\text{orb}}^{(2N+1)/3} \right)^2. \quad (14)$$

In Fig. 12, the blue curve before $-8000 M$ corresponds to the LHS, the blue curve after $-3000 M$ corresponds to the RHS, and the region between $-8000 M$ and $-3000 M$ is where the two effects are comparable. For cases with different but small eccentricities, we expect the error curve after $-3000 M$ to be similar to that in Fig. 12, and the curve before $-8000 M$ to be parallel to the blue curve in Fig. 12, but with a vertical shift. Since the curve after $-3000 M$ is steep and the curve before $-8000 M$ is gradual, the point where the left and right part of the curve meet with each other (which is the best location for the matching window) is not very sensitive to the eccentricity of the system.

At the current state-of-the-art NR accuracy, and for \mathcal{E} between PN and NR in the test window of $\sim 10^{-4}$, the minimal choice for a matching window for spin-aligned systems would be at least 5 orbits long and ending $3000 M$ before merger. This minimal choice will become longer and earlier if higher-accuracy hybrids are desired, and if the accuracy of the waveforms improves. Matching windows longer than 20 orbits or ending earlier than $8000 M$ are not beneficial given the current state of the art, but would be beneficial if the residual eccentricity of NR waveforms were decreased or if eccentric PN waveforms were used for hybridization.

B. Precessing systems

In Sec. VI B, we established that the error in hybridizing precessing systems mainly results from the absence of higher-order PN spin terms. Because PN error decreases with smaller frequencies, we anticipate smaller hybridization errors at earlier times. To determine the best location of the matching window, we plot the hybridization error of system SXS:BBH:2621 in the matching window versus orbital angular velocity Ω_{orb} in Fig. 19. This system has $\chi_p = 0.49$. Since the leading missing PN precession-related spin terms are expected to be $\propto (S_{\perp}/M^2)^{\alpha} v^{\beta}$, where $v = (\Omega_{\text{orb}} M)^{1/3}$ is the PN expansion parameter, we can get the indices α and β by fitting the points in Fig. 15 and Fig. 19, respectively. Then we can get an empirical formula $\mathcal{E} \sim 5 \times 10^8 \times (S_{\perp}/M^2)^{3.8} \Omega_{\text{orb}}^5$, or

$$\Omega_{\text{orb}} \lesssim 0.018 \mathcal{E}^{0.2} (S_{\perp}/M^2)^{-0.76}. \quad (15)$$

Once a required precision \mathcal{E} for a 10-orbit long window is given, we can use Eq. (15) to determine the average orbital angular velocity of the matching window. From the average orbital angular velocity one can figure out the end time of the matching window. Note that both Figs. 15 and 19 use a 10-orbit long matching window, because it is short enough to avoid being dominated by long-term accumulated phase error, and also limits significant frequency changes within the window.

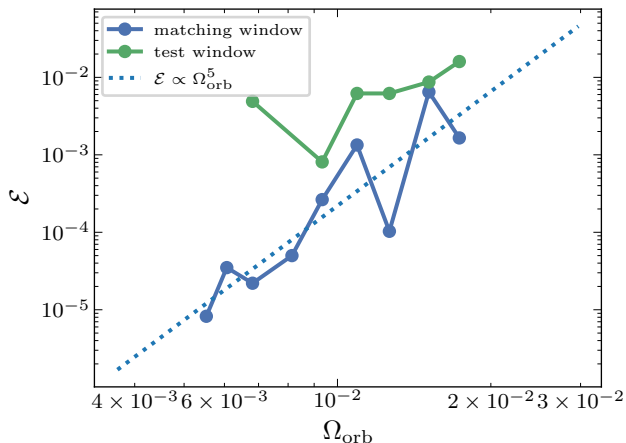


FIG. 19. The L^2 normalized error \mathcal{E} in the matching window as a function of orbital angular velocity for system SXS:BBH:2621. The matching window is 10 orbits long, but the end time of the matching window is varied, and the orbital angular velocity is the mean value over the matching window. The test window is 10 orbits long, and the center of the test window (in number of orbits) is 30 orbits earlier than the center of the matching window.

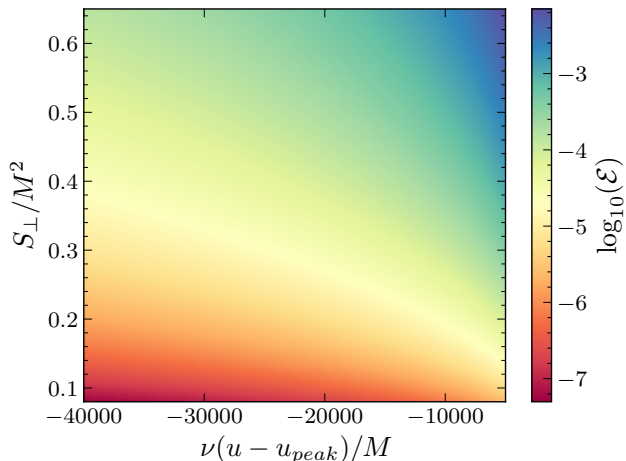


FIG. 20. The predicted L^2 normalized error \mathcal{E} for a 10-orbit matching window based on Eq. 15. The horizontal axis is the approximate center of the matching window, where $\nu = m_1 m_2 / (m_1 + m_2)^2$, and u is the retarded time. The vertical axis is the maximum of the in-plane component of the two dimensionless spin momenta.

We also plot the predicted \mathcal{E} given a 10-orbit window in terms of the end time of the matching window and S_{\perp}/M^2 in Fig. 20. Here we used leading order PN to substitute orbital angular velocity with time: $\nu(u - u_{\text{peak}}) = \frac{5}{256} \Omega_{\text{orb}}^{-8/3}$, where $\nu = m_1 m_2 / (m_1 + m_2)^2$.

Determining the ideal matching window length for precessing systems through experiments is challenging, unlike the spin-aligned cases. This challenge arises because the

recommended end time for the matching window is significantly earlier for systems with large spin. Consequently, generating a complete precession cycle before this end time is impractical using NR simulations. However, considering that the error is primarily governed by the PN spin terms, which diminish at earlier times (in contrast to errors stemming from non-zero eccentricity, which worsen at earlier times), it is anticipated that longer matching windows are more beneficial for precessing systems.

C. Short waveforms

Unfortunately, most of the NR waveforms in current catalogs are not long enough to meet the minimal criteria for a matching window discussed in Sec. VII. In this scenario, it is important to note that the optimized PN parameters and BMS frame computed by the hybridization procedure may be biased by the breakdown of PN. Additionally, there is a risk of overfitting when optimizing the PN parameters and inertial frames from too-small a matching window.

To better understand these issues, we simulate an “8000 M ” waveform scenario. We set the start time of the matching window to be $-8000 M$ and test the hybridization results using a 10-orbit long test window positioned between 30 and 40 orbits before $-8000 M$. The results are shown in Fig. 21 and Fig. 22.

In Fig. 21, we display \mathcal{E} for different lengths of the matching window for system SXS:BBH:2617 for this scenario. The dotted lines in the upper panel show that the error in the matching window for extrapolated waveforms is independent of the length of the matching window because the error is dominated by the incorrect gravitational-wave memory in the extrapolated waveforms. The solid lines show that as the length of the matching window becomes shorter, the error in the matching window becomes smaller. However, by comparing the blue and green curves between the upper and lower panels, we can see that smaller error in the matching window does not mean smaller error in the test window. To more intuitively show the relation between the error in the matching window and the test window, we take all the blue and green points in Fig. 21, and plot them in Fig. 22. We can see that the errors in the test window and matching window show no unambiguous trend. This non-correlation of the matching and test window errors suggests that although we can always get a small error in the matching window if the matching window is short, it is not gaining us more information about the PN parameters and BMS frame to improve the error in the test window.

So, if we do not have NR waveforms that are long enough to meet the criteria outlined in Sec. VII A and Sec. VII B, the hybridization could be biased by the breakdown of PN and overfitting.

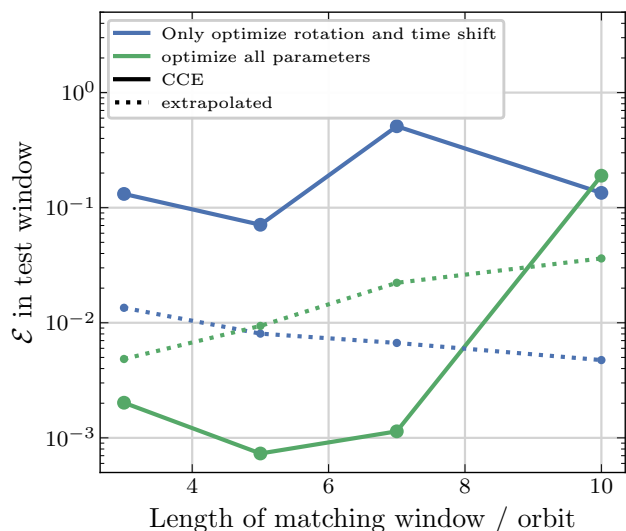
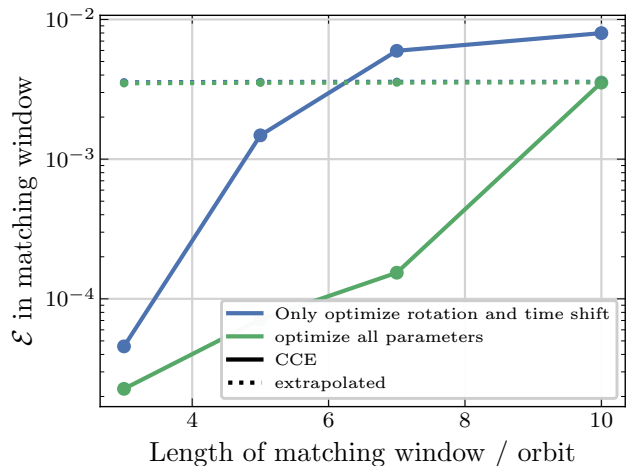


FIG. 21. The L^2 normalized error \mathcal{E} for different lengths of the matching window for system SXS:BBH:2617. The test window is between 30 and 40 orbits before $-8000 M$. We fix the start time of the matching window to be $8000 M$ before merger. The upper and lower panel show \mathcal{E} in the matching window and the test window, respectively. The dotted curves use extrapolated NR waveforms, while the solid curves use CCE NR waveforms. All the curves are obtained after adjusting the 3-D rotation and time shift, and all the curves using CCE waveforms are obtained after mapping to the PN BMS frame. In addition to the 3-D rotation and time shift, the green curves optimize all 12 parameters, which is the full hybridization procedure described in Section IV.

VIII. CONCLUSIONS

We provide a BBH waveform hybridization routine that includes every spin-weighted spherical harmonic mode with $-\ell \leq m \leq \ell$ for $\ell \leq 8$ as well as memory effects, and utilizes BMS frame fixing and PN parameter optimization. The L^2 normalized error \mathcal{E} between PN and NR waveforms in a 10-orbit *matching* window is roughly 10^{-7} for spin-

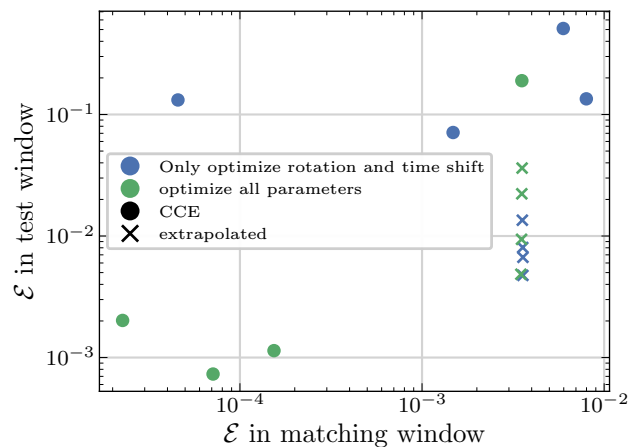


FIG. 22. The L^2 normalized error \mathcal{E} for different lengths of the matching window for system SXS:BBH:2617. The test window is between 30 and 40 orbits before $-8000 M$. We fix the start time of the matching window to be $8000 M$ before merger. The crosses use extrapolated NR waveforms, while the dots use CCE NR waveforms. All the data are obtained after adjusting the 3-D rotation and time shift, and all the dots using CCE waveforms are obtained after mapping to the PN BMS frame. The blue and the green data points are the same data as the blue and green curves in Fig. 21. The extrapolated waveforms all have the same error in the matching window, because for those waveforms the matching window error is dominated by incorrect gravitational-wave memory.

aligned systems, and roughly 10^{-5} for precessing systems.

However, a more informative measure of the accuracy of a hybridized waveform is the PN-NR difference in a *test* window that is earlier than the matching window so that PN errors are small, and that does not overlap with the matching window so that we are not actively minimizing the PN-NR difference there. In a test window that is 10 orbits long and 30 orbits earlier than the matching window, we can reduce the normalized PN-NR difference to less than $\sim 10^{-4}$ for spin-aligned systems, as shown by the solid green curve in Fig. 17. This corresponds to $\sim 10^{-2}$ absolute difference between PN and NR waveforms in this interval. Again, we note that these numbers are not directly comparable to the frequency-domain mismatches used in GW data analysis, even assuming a flat noise curve, because the test and matching windows will not generally encompass the entire detectable waveform. At best, these numbers constitute lower bounds for the full mismatch. However, they do suggest that even for spin-aligned systems the results may be inadequate for high-SNR events in future detectors such as Cosmic Explorer and LISA.

For spin-aligned systems, the error in the test window can likely be decreased somewhat by using higher-accuracy NR waveforms, since the green curves in Fig. 17 are roughly decreasing with NR resolution. However, the error is ultimately limited by trying to match zero-eccentricity PN waveforms with small but non-zero eccen-

tricity NR waveforms. To achieve test window differences much better than $\mathcal{E} \lesssim 10^{-4}$ for spin-aligned systems, it will be necessary to either reduce the residual eccentricity of the NR waveforms or to use an eccentric PN model for hybridization.

While we recommend optimizing the intrinsic PN parameters in addition to the BMS frame parameters, we find that this optimization can sometimes lead to fractional differences in mass ratio and spin up to $\sim 10^{-1}$ between NR and the best-fit PN waveform (see Fig. 11). This could arise from overfitting, where missing PN terms or NR truncation errors can be absorbed into the PN parameter optimization. This can be more significant for most current NR waveforms as they are typically much shorter than the ones considered here (see Sec. VII C for tests using NR waveforms starting $8000M$ before merger). As PN continues to improve and NR waveforms become longer, we expect these differences to decrease. In the meantime, caution is warranted when varying the intrinsic PN parameters for short NR waveforms.

In principle, if one had perfect and exactly quasi-circular NR waveforms, the matching window should be chosen as early as possible (to avoid matching at late times near merger where PN becomes inaccurate), and it should be chosen as long as possible (so that one can match over a longer stretch of data and thus obtain a better fit). For current NR waveforms, and for spin-aligned systems, we find that to achieve $\mathcal{E} \sim 10^{-4}$ differences in the test window, the matching window should be at least 5 orbits long and should end at least $3000M$ before merger. While in principle a longer and earlier matching window should be better, we find that matching windows longer than 20 orbits or ending earlier than $8000M$ are not beneficial because the error is then dominated by the nonzero eccentricity of the NR waveforms as described above. By using either smaller-eccentricity NR waveforms or employing eccentric PN, it should be possible to further improve hybridization by using longer and earlier matching windows.

Hybridization of precessing systems is much more difficult than spin-aligned systems, because the current PN waveforms for precessing systems are much less accurate than for spin-aligned systems. For precessing systems, the error in the hybrid is dominated by the lack of precession-related spin-spin terms in the PN model. Unlike the error caused by non-zero eccentricity, the error stemming from PN terms diminishes at earlier times. So there is no optimal choice of the matching window even in the entire $10^5 M$ span of the NR waveforms in the SXS catalog, and it always improves the hybridization by using matching windows as long and early as possible. We provide a formula, Eq. 15, and a plot, Fig. 20, as a guide for choosing a matching window for precessing hybrids. The recommended end time for the matching window is significantly earlier for systems with large spin.

ACKNOWLEDGMENTS

We thank Sizheng Ma, Nils Deppe, Qing Dai and Harald Pfeiffer for useful discussions. Computations for this work were performed on the Wheeler cluster at Caltech, which is supported by the Sherman Fairchild Foundation and by Caltech, Resnick High Performance Computing (HPC) Cluster at the Caltech High Performance Computing Center, Frontera at the Texas Advanced Computing Center, and Urania HPC system at the Max Planck Computing and Data Facility. This work was supported in part by the Sherman Fairchild Foundation, by NSF Grants PHY-2207342 and OAC-2209655 at Cornell, and by NSF Grants PHY-2309211, PHY-2309231, and OAC-2209656 at Caltech. The work of L.C.S. was partially supported by NSF CAREER Award PHY-2047382 and a Sloan Foundation Research Fellowship. V.V. acknowledges support from NSF Grant No. PHY-2309301; UMass Dartmouth's Marine and Undersea Technology (MUST) Research Program funded by the Office of Naval Research (ONR) under Grant No. N00014-23-1-2141; and the European Union's Horizon 2020 research and innovation program under the Marie Skłodowska-Curie grant agreement No. 896869.

REFERENCES

- [1] B. P. Abbott *et al.* (LIGO Scientific, Virgo), GW150914: The Advanced LIGO Detectors in the Era of First Discoveries, *Phys. Rev. Lett.* **116**, 131103 (2016), arXiv:1602.03838 [gr-qc].
- [2] B. P. Abbott *et al.* (LIGO Scientific, Virgo), Binary Black Hole Mergers in the first Advanced LIGO Observing Run, *Phys. Rev. X* **6**, 041015 (2016), [erratum: *Phys. Rev. X*, no.3,039903(2018)], arXiv:1606.04856 [gr-qc].
- [3] B. P. Abbott *et al.* (LIGO Scientific, Virgo), GW150914: First results from the search for binary black hole coalescence with Advanced LIGO, *Phys. Rev. D* **93**, 122003 (2016), arXiv:1602.03839 [gr-qc].
- [4] B. P. Abbott *et al.* (LIGO Scientific, Virgo), Properties of the Binary Black Hole Merger GW150914, *Phys. Rev. Lett.* **116**, 241102 (2016), arXiv:1602.03840 [gr-qc].
- [5] B. P. Abbott *et al.* (LIGO Scientific, Virgo), GW170817: Observation of Gravitational Waves from a Binary Neutron Star Inspiral, *Phys. Rev. Lett.* **119**, 161101 (2017), arXiv:1710.05832 [gr-qc].
- [6] B. P. Abbott *et al.* (LIGO Scientific, Virgo), Binary Black Hole Population Properties Inferred from the First and Second Observing Runs of Advanced LIGO and Advanced Virgo, *Astrophys. J. Lett.* **882**, L24 (2019), arXiv:1811.12940 [astro-ph.HE].
- [7] R. Abbott *et al.* (LIGO Scientific, VIRGO, KAGRA), GWTC-3: Compact Binary Coalescences Observed by LIGO and Virgo During the Second Part of the Third Observing Run, arXiv:2111.03606 [gr-qc].
- [8] R. Abbott *et al.* (LIGO Scientific, Virgo), GW190412: Observation of a Binary-Black-Hole Coalescence with Asymmetric Masses, *Phys. Rev. D* **102**, 043015 (2020), arXiv:2004.08342 [astro-ph.HE].
- [9] R. Abbott *et al.* (LIGO Scientific, VIRGO, KAGRA), The population of merging compact binaries inferred using

- gravitational waves through GWTC-3, [arXiv:2111.03634 \[astro-ph.HE\]](#).
- [10] B. P. Abbott *et al.* (LIGO Scientific, Virgo), Tests of general relativity with GW150914, *Phys. Rev. Lett.* **116**, 221101 (2016), [Erratum: *Phys. Rev. Lett.* 121,no.12,129902(2018)], [arXiv:1602.03841 \[gr-qc\]](#).
- [11] B. P. Abbott *et al.* (LIGO Scientific, Virgo), Tests of General Relativity with the Binary Black Hole Signals from the LIGO-Virgo Catalog GWTC-1, *Phys. Rev.* **D100**, 104036 (2019), [arXiv:1903.04467 \[gr-qc\]](#).
- [12] R. Abbott *et al.* (LIGO Scientific, VIRGO, KAGRA), Tests of General Relativity with GWTC-3, [arXiv:2112.06861 \[gr-qc\]](#).
- [13] J. Aasi *et al.* (LIGO Scientific), Advanced LIGO, *Class. Quant. Grav.* **32**, 074001 (2015), [arXiv:1411.4547 \[gr-qc\]](#).
- [14] B. P. Abbott *et al.* (LIGO Scientific, Virgo), GWTC-1: A Gravitational-Wave Transient Catalog of Compact Binary Mergers Observed by LIGO and Virgo during the First and Second Observing Runs, *Phys. Rev.* **X9**, 031040 (2019), [arXiv:1811.12907 \[astro-ph.HE\]](#).
- [15] F. Acernese *et al.* (Virgo), Advanced Virgo: a second-generation interferometric gravitational wave detector, *Class. Quant. Grav.* **32**, 024001 (2015), [arXiv:1408.3978 \[gr-qc\]](#).
- [16] T. Akutsu *et al.* (KAGRA), KAGRA: 2.5 Generation Interferometric Gravitational Wave Detector, *Nature Astron.* **3**, 35 (2019), [arXiv:1811.08079 \[gr-qc\]](#).
- [17] M. Punturo *et al.*, The Einstein Telescope: A third-generation gravitational wave observatory, *Proceedings, 14th Workshop on Gravitational wave data analysis (GWDAW-14): Rome, Italy, January 26-29, 2010*, *Class. Quant. Grav.* **27**, 194002 (2010).
- [18] D. Reitze *et al.*, Cosmic Explorer: The U.S. Contribution to Gravitational-Wave Astronomy beyond LIGO, *Bull. Am. Astron. Soc.* **51**, 035 (2019), [arXiv:1907.04833 \[astro-ph.IM\]](#).
- [19] P. Amaro-Seoane *et al.*, eLISA/NGO: Astrophysics and cosmology in the gravitational-wave millihertz regime, *GW Notes* **6**, 4 (2013), [arXiv:1201.3621 \[astro-ph.CO\]](#).
- [20] J. Luo *et al.* (TianQin), TianQin: a space-borne gravitational wave detector, *Class. Quant. Grav.* **33**, 035010 (2016), [arXiv:1512.02076 \[astro-ph.IM\]](#).
- [21] W.-R. Hu and Y.-L. Wu, The Taiji Program in Space for gravitational wave physics and the nature of gravity, *Natl. Sci. Rev.* **4**, 685 (2017).
- [22] M. Maggiore *et al.*, Science Case for the Einstein Telescope, *JCAP* **03**, 050, [arXiv:1912.02622 \[astro-ph.CO\]](#).
- [23] P. Amaro-Seoane *et al.*, Low-frequency gravitational-wave science with eLISA/NGO, *Class. Quant. Grav.* **29**, 124016 (2012), [arXiv:1202.0839 \[gr-qc\]](#).
- [24] M. Bailes, B. Berger, P. Brady, *et al.*, Gravitational-wave physics and astronomy in the 2020s and 2030s, *Nat Rev Phys* **3**, 344–366 (2021).
- [25] L. Santamaria *et al.*, Matching post-Newtonian and numerical relativity waveforms: systematic errors and a new phenomenological model for non-precessing black hole binaries, *Phys. Rev. D* **82**, 064016 (2010), [arXiv:1005.3306 \[gr-qc\]](#).
- [26] I. MacDonald, S. Nissanke, H. P. Pfeiffer, and H. P. Pfeiffer, Suitability of post-Newtonian/numerical-relativity hybrid waveforms for gravitational wave detectors, *Theory meets data analysis at comparable and extreme mass ratios. Proceedings, Conference, NRDA/CAPRA 2010, Waterloo, Canada, June 20-26, 2010*, *Class. Quant. Grav.* **28**, 134002 (2011), [arXiv:1102.5128 \[gr-qc\]](#).
- [27] M. Boyle, Uncertainty in hybrid gravitational waveforms: Optimizing initial orbital frequencies for binary black-hole simulations, *Phys. Rev.* **D84**, 064013 (2011), [arXiv:1103.5088 \[gr-qc\]](#).
- [28] I. MacDonald, A. H. Mroue, H. P. Pfeiffer, M. Boyle, L. E. Kidder, M. A. Scheel, B. Szilagyi, and N. W. Taylor, Suitability of hybrid gravitational waveforms for unequal-mass binaries, *Phys. Rev.* **D87**, 024009 (2013), [arXiv:1210.3007 \[gr-qc\]](#).
- [29] V. Varma, S. E. Field, M. A. Scheel, J. Blackman, L. E. Kidder, and H. P. Pfeiffer, Surrogate model of hybridized numerical relativity binary black hole waveforms, *Phys. Rev.* **D99**, 064045 (2019), [arXiv:1812.07865 \[gr-qc\]](#).
- [30] J. Sadiq, Y. Zlochower, R. O’Shaughnessy, and J. Lange, Hybrid waveforms for generic precessing binaries for gravitational-wave data analysis, *Phys. Rev. D* **102**, 024012 (2020), [arXiv:2001.07109 \[gr-qc\]](#).
- [31] K. Mitman *et al.*, Fixing the BMS frame of numerical relativity waveforms with BMS charges, *Phys. Rev. D* **106**, 084029 (2022), [arXiv:2208.04356 \[gr-qc\]](#).
- [32] S. S. Bavera, T. Fragos, Y. Qin, E. Zapartas, C. J. Neijssel, I. Mandel, A. Batta, S. M. Gaebel, C. Kimball, and S. Stevenson, The origin of spin in binary black holes: Predicting the distributions of the main observables of Advanced LIGO, *Astron. Astrophys.* **635**, A97 (2020), [arXiv:1906.12257 \[astro-ph.HE\]](#).
- [33] L. Ma and J. Fuller, Tidal Spin-up of Black Hole Progenitor Stars, *Astrophys. J.* **952**, 53 (2023), [arXiv:2305.08356 \[astro-ph.HE\]](#).
- [34] D. Gerosa, E. Berti, R. O’Shaughnessy, K. Belczynski, M. Kesden, D. Wysocki, and W. Gladysz, Spin orientations of merging black holes formed from the evolution of stellar binaries, *Phys. Rev.* **D98**, 084036 (2018), [arXiv:1808.02491 \[astro-ph.HE\]](#).
- [35] V. Tiwari, S. Fairhurst, and M. Hannam, Constraining black-hole spins with gravitational wave observations, *Astrophys. J.* **868**, 140 (2018), [arXiv:1809.01401 \[gr-qc\]](#).
- [36] C. L. Rodriguez, M. Zevin, C. Pankow, V. Kalogera, and F. A. Rasio, Illuminating Black Hole Binary Formation Channels with Spins in Advanced LIGO, *Astrophys. J. Lett.* **832**, L2 (2016), [arXiv:1609.05916 \[astro-ph.HE\]](#).
- [37] N. T. Bishop, R. Gomez, L. Lehner, and J. Winicour, Cauchy-characteristic extraction in numerical relativity, *Phys. Rev.* **D54**, 6153 (1996), [arXiv:gr-qc/9705033 \[gr-qc\]](#).
- [38] J. Winicour, Characteristic Evolution and Matching, *Living Rev. Rel.* **12**, 3 (2009), [arXiv:0810.1903 \[gr-qc\]](#).
- [39] M. C. Babiuc, J. Winicour, and Y. Zlochower, Binary Black Hole Waveform Extraction at Null Infinity, *Class. Quant. Grav.* **28**, 134006 (2011), [arXiv:1106.4841 \[gr-qc\]](#).
- [40] J. Moxon, M. A. Scheel, and S. A. Teukolsky, Improved Cauchy-characteristic evolution system for high-precision numerical relativity waveforms, *Phys. Rev. D* **102**, 044052 (2020), [arXiv:2007.01339 \[gr-qc\]](#).
- [41] J. Moxon, M. A. Scheel, S. A. Teukolsky, N. Deppe, N. Fischer, F. Hébert, L. E. Kidder, and W. Throwe, SpECTRE Cauchy-characteristic evolution system for rapid, precise waveform extraction, *Phys. Rev. D* **107**, 064013 (2023), [arXiv:2110.08635 \[gr-qc\]](#).
- [42] M. Boyle and A. H. Mroue, Extrapolating gravitational-wave data from numerical simulations, *Phys. Rev.* **D80**, 124045 (2009), [arXiv:0905.3177 \[gr-qc\]](#).
- [43] SXS Collaboration, The SXS collaboration catalog of

- gravitational waveforms, <http://www.black-holes.org/waveforms>.
- [44] J. Sadiq *et al.*, Hybrid waveforms for generic precessing binaries for gravitational-wave data analysis, *Physical Review D* **102**, 10.1103/physrevd.102.024012 (2020).
- [45] D. Sun, Nrnphybridization, <https://github.com/dongzesun/NRPNHybridization>.
- [46] L. Blanchet, Gravitational Radiation from Post-Newtonian Sources and Inspiralling Compact Binaries, *Living Rev. Rel.* **17**, 2 (2014), arXiv:1310.1528 [gr-qc].
- [47] L. Blanchet, G. Faye, Q. Henry, F. Larrouturou, and D. Trestini, Gravitational-wave flux and quadrupole modes from quasicircular nonspinning compact binaries to the fourth post-Newtonian order, *Phys. Rev. D* **108**, 064041 (2023), arXiv:2304.11186 [gr-qc].
- [48] R. Fujita, Gravitational Waves from a Particle in Circular Orbits around a Schwarzschild Black Hole to the 22nd Post-Newtonian Order, *Prog. Theor. Phys.* **128**, 971 (2012), arXiv:1211.5535 [gr-qc].
- [49] S. Marsat, A. Bohé, L. Blanchet, and A. Buonanno, Next-to-leading tail-induced spin-orbit effects in the gravitational radiation flux of compact binaries, *Class. Quant. Grav.* **31**, 025023 (2014), arXiv:1307.6793 [gr-qc].
- [50] A. Bohé, G. Faye, S. Marsat, and E. K. Porter, Quadratic-in-spin effects in the orbital dynamics and gravitational-wave energy flux of compact binaries at the 3PN order, *Class. Quant. Grav.* **32**, 195010 (2015), arXiv:1501.01529 [gr-qc].
- [51] S. Marsat, Cubic order spin effects in the dynamics and gravitational wave energy flux of compact object binaries, *Class. Quant. Grav.* **32**, 085008 (2015), arXiv:1411.4118 [gr-qc].
- [52] A. Bohe, S. Marsat, G. Faye, and L. Blanchet, Next-to-next-to-leading order spin-orbit effects in the near-zone metric and precession equations of compact binaries, *Class. Quant. Grav.* **30**, 075017 (2013), arXiv:1212.5520 [gr-qc].
- [53] L. Blanchet, G. Faye, B. R. Iyer, and S. Sinha, The Third post-Newtonian gravitational wave polarisations and associated spherical harmonic modes for inspiralling compact binaries in quasi-circular orbits, *Class. Quant. Grav.* **25**, 165003 (2008), [Erratum: *Class. Quant. Grav.* **29**, 239501 (2012)], arXiv:0802.1249 [gr-qc].
- [54] G. Faye, S. Marsat, L. Blanchet, and B. R. Iyer, The third and a half post-Newtonian gravitational wave quadrupole mode for quasi-circular inspiralling compact binaries, *Class. Quant. Grav.* **29**, 175004 (2012), arXiv:1204.1043 [gr-qc].
- [55] G. Faye, L. Blanchet, and B. R. Iyer, Non-linear multipole interactions and gravitational-wave octupole modes for inspiralling compact binaries to third-and-a-half post-Newtonian order, *Class. Quant. Grav.* **32**, 045016 (2015), arXiv:1409.3546 [gr-qc].
- [56] O. M. Moreschi, Supercenter of Mass System at Future Null Infinity, *Class. Quant. Grav.* **5**, 423 (1988).
- [57] H. Bondi, M. G. J. van der Burg, and A. W. K. Metzner, Gravitational waves in general relativity. 7. Waves from axisymmetric isolated systems, *Proc. Roy. Soc. Lond.* **A269**, 21 (1962).
- [58] R. K. Sachs, Gravitational waves in general relativity. 8. Waves in asymptotically flat space-times, *Proc. Roy. Soc. Lond.* **A270**, 103 (1962).
- [59] R. Sachs, Asymptotic symmetries in gravitational theory, *Phys. Rev.* **128**, 2851 (1962).
- [60] M. Boyle, D. Iozzo, L. Stein, A. Khairnar, H. Rüter, M. Scheel, V. Varma, and K. Mitman, *scri* (2023).
- [61] M. Boyle, Transformations of asymptotic gravitational-wave data, *Phys. Rev.* **D93**, 084031 (2016), arXiv:1509.00862 [gr-qc].
- [62] K. Mitman *et al.*, Fixing the BMS frame of numerical relativity waveforms, *Phys. Rev. D* **104**, 024051 (2021), arXiv:2105.02300 [gr-qc].
- [63] E. T. Newman and R. Penrose, Note on the Bondi-Metzner-Sachs group, *J. Math. Phys.* **7**, 863 (1966).
- [64] M. Boyle, How should spin-weighted spherical functions be defined?, *J. Math. Phys.* **57**, 092504 (2016), arXiv:1604.08140 [gr-qc].
- [65] The Spectral Einstein Code, <http://www.black-holes.org/SpEC.html>.
- [66] N. Deppe, W. Throwe, L. E. Kidder, N. L. Vu, F. Hébert, J. Moxon, C. Armaza, M. S. Bonilla, Y. Kim, P. Kumar, G. Lovelace, A. Macedo, K. C. Nelli, E. O'Shea, H. P. Pfeiffer, M. A. Scheel, S. A. Teukolsky, N. A. Wittek, *et al.*, *SpECTRE v2023.05.16*, 10.5281/zenodo.7942177 (2023).
- [67] P. Schmidt, F. Ohme, and M. Hannam, Towards models of gravitational waveforms from generic binaries II: Modelling precession effects with a single effective precession parameter, *Phys. Rev. D* **91**, 024043 (2015), arXiv:1408.1810 [gr-qc].
- [68] M. Boyle *et al.*, The SXS Collaboration catalog of binary black hole simulations, *Class. Quant. Grav.* **36**, 195006 (2019), arXiv:1904.04831 [gr-qc].
- [69] J. Blackman, S. E. Field, M. A. Scheel, C. R. Galley, D. A. Hemberger, P. Schmidt, and R. Smith, A Surrogate Model of Gravitational Waveforms from Numerical Relativity Simulations of Precessing Binary Black Hole Mergers, *Phys. Rev.* **D95**, 104023 (2017), arXiv:1701.00550 [gr-qc].
- [70] P. Virtanen, R. Gommers, T. E. Oliphant, M. Haberland, T. Reddy, D. Cournapeau, E. Burovski, P. Peterson, W. Weckesser, J. Bright, S. J. van der Walt, M. Brett, J. Wilson, K. J. Millman, N. Mayorov, A. R. J. Nelson, E. Jones, R. Kern, E. Larson, C. J. Carey, Í. Polat, Y. Feng, E. W. Moore, J. VanderPlas, D. Laxalde, J. Perktold, R. Cimrman, I. Henriksen, E. A. Quintero, C. R. Harris, A. M. Archibald, A. H. Ribeiro, F. Pedregosa, P. van Mulbregt, and SciPy 1.0 Contributors, *SciPy 1.0: Fundamental Algorithms for Scientific Computing in Python*, *Nature Methods* **17**, 261 (2020).
- [71] M. A. Branch, T. F. Coleman, and Y. Li, A subspace, interior, and conjugate gradient method for large-scale bound-constrained minimization problems, *SIAM Journal on Scientific Computing* **21**, 1 (1999).
- [72] M. Boyle, Angular velocity of gravitational radiation from precessing binaries and the corotating frame, *Phys. Rev.* **D87**, 104006 (2013), arXiv:1302.2919 [gr-qc].
- [73] C. J. Woodford, M. Boyle, and H. P. Pfeiffer, Compact Binary Waveform Center-of-Mass Corrections, *Phys. Rev. D* **100**, 124010 (2019), arXiv:1904.04842 [gr-qc].
- [74] M. A. Shaikh, V. Varma, H. P. Pfeiffer, A. Ramos-Buades, and M. van de Meent, Defining eccentricity for gravitational wave astronomy, pypi.org/project/gw_eccentricity, arXiv:2302.11257 [gr-qc].
- [75] M. Ebersold, Y. Boetzel, G. Faye, C. K. Mishra, B. R. Iyer, and P. Jetzer, Gravitational-wave amplitudes for compact binaries in eccentric orbits at the third post-Newtonian order: Memory contributions, *Phys. Rev. D* **100**, 084043 (2019), arXiv:1906.06263 [gr-qc].
- [76] B. Moore, M. Favata, K. G. Arun, and C. K. Mishra, Gravitational-wave phasing for low-eccentricity inspi-

ralling compact binaries to 3PN order, *Phys. Rev. D*
93, 124061 (2016), arXiv:1605.00304 [gr-qc].